Chemical Engineering Journal 525 (2025) 170739

Contents lists available at ScienceDirect

Chemical Engineering Journal

journal homepage: www.elsevier.com/locate/cej

Strong yet mechanically flexible thick necked aerogels fabricated via in situ-catalyzed epoxy-thiol polymerization with necking enhancement: A finite element simulation and wastewater treatment applications

Vinayak G. Parale [a,b,c,1], Haryeong Choi [a,1], Varsha D. Phadtare [a,b], Rushikesh P. Dhavale [a], Younghun Kim [a], Akshay A. Ransing [a], Ivan I. Smalyukh [c,d], Michele Meo [e,*], Hyung-Ho Park [a,b,**]

[a] Department of Materials Science and Engineering, Yonsei University, Seoul, 03722, Republic of Korea
[b] Aerogel Materials Research Center, Yonsei University, Seoul, 03722, Republic of Korea
[c] International Institute for Sustainability with Knotted Chiral Meta Matter, Hiroshima University, 1-3-1 Kagamiyama, Higashi-Hiroshima, Hiroshima, 739-8526, Japan
[d] Department of Physics, University of Colorado, Boulder, CO, USA
[e] Department of Aeronautics and Astronautics, University of Southampton, Southampton, SO16 7QF, UK

ARTICLE INFO

Keywords:
Thick necked aerogel
Epoxy-thiol polymerization
Necking enhancement
Strong yet flexible
Finite element simulation
Water treatment

ABSTRACT

Ultralight organic-inorganic-crosslinked aerogels that are strong yet mechanically flexible and multifunctional are attractive for use in versatile applications. However, conventional resorcinol-formaldehyde (RF)-based aerogels are either strong or flexible while Si-based aerogels are brittle, and both have limited long-term practicability. Therefore, the fabrication of mechanically strong yet flexible RFSi-crosslinked aerogels containing S-functional groups (Si) obtained via a new synthetic route involving epoxy-thiol polymerization and necking enhancement is presented herein. Three hybrid RF-Si aerogels that are soft, mechanically strong, and mechanically strong yet flexible are possible according to the synthesis conditions and the amount of neck region enhancement. An epoxy-thiol-polymerized RF-Si aerogel using an ethanol supercritical drying (SCD) process (S-RFSi_SCD) possesses ultralow density (~0.050 g·cm^{-3}), excellent mechanical properties with 50 % reversible compression strain, excellent fatigue resistance, high compressive modulus (5.65 MPa), excellent room temperature thermal insulating property (0.026 W·m^{-1} K^{-1}), and multifunctionality due to the presence of S-functional groups. Finite element simulations were employed to investigate the deformation behavior with neck enhancement. When used as an adsorbent, S-RFSi_SCD aerogel shows excellent Hg^{2+} adsorption (~699.3 mg/g) and acceptable methylene blue dye adsorption (~105.48 mg/g). This successfully applied novel synthetic approach efficiently provides mechanically strong yet flexible and multifunctional S-functionalized Polymer-Si-crosslinked aerogels addressing limitations of mechanical properties of RF (strong or flexible), and Si aerogel (brittleness). This advancement enhances the sustained viability and adaptability of aerogels for high-performance applications in various industries, including thermal insulation, flexible electronics, pollutant filtration, and medical devices.

1. Introduction

Aerogels with thermal insulating properties that are both robust and mechanically flexible are necessary for aerospace applications. Ceramic aerogels are appealing thermal insulation materials because of their low density, low thermal conductivity, and outstanding thermal stability. [1,2] However, because ceramics are brittle and have weak intergranular necking junctions, traditional ceramic aerogels made of oxide nanoparticles are often weak and brittle. [3,4] Although both polymer-crosslinking and fiber-reinforcement can provide ceramic aerogels with increased strength and deformability, the products can still be thermally unstable or prone to severe dust release, which makes them unsuitable

* Corresponding author.
** Correspondence to: H.-H. Park, Department of Materials Science and Engineering, Yonsei University, Seoul, 03722, Republic of Korea.
E-mail addresses: m.meo@soton.ac.uk (M. Meo), hhpark@yonsei.ac.kr (H.-H. Park).
[1] Authors contributed equally to this manuscript.

https://doi.org/10.1016/j.cej.2025.170739
Received 29 September 2025; Received in revised form 3 November 2025; Accepted 9 November 2025
Available online 10 November 2025

for use in real-world applications. [5–7] Many materials found in nature, such as silkworm cocoons, are lightweight, robust, resilient, and thermally insulating. [8] The silkworm cocoon's naturally developed high-strength yet flexible silk and its silk-assembled laminated microstructure are credited with giving it such appealing features. [9,10]

The morphological characteristics of aerogels, such as a high pore volume, optimized void size, and porous solid walls, can bestow them with multifunctionality. This is because these features confine thermal conduction through gas voids and a dissipative path for heat transport through the low solid fraction under phonon scattering. Nevertheless, ceramic aerogels fall short of the high standards for building insulation materials since they are inherently brittle and have a tendency to lose their natural texture under compression. [11–13] Therefore, strong elasticity and excellent reversibility under mechanical stress are needed to prevent ceramic aerogels from breaking down in response to substantial compressive pressure. [14] Although using organic polymers to provide crosslinking is one method of increasing the mechanical elasticity of ceramic aerogels, [15] the effectiveness of the latter as thermal insulators can be diminished by incorporating the former.

An Si-based aerogel created via a sol-gel process is made up of a fractal pearl necklace-like network in which the neck area between secondary particles serves as building blocks, [16,17] thereby imparting fragility to the aerogel skeletal structure. The neck region, which is formed by the agglomeration of particles during the gelation process followed by aging, [18] can be strengthened by the dissolution and precipitation of Si within the aerogel network during the aging period. This improves the mechanical strength of the resulting aerogel but no other possible parameters of interest. However, pristine Si aerogels comprising continuous Si-O-Si chains lack a degree of motion, thereby making them incapable of exhibiting elastoplastic deformability. [19,20] To solve this issue, many researchers have focused on the synthesis of Si aerogels using organosiloxanes containing a varying number of alkyl groups, [21–23] which provides a degree of deformability without changing the mechanical strength. [23] Nanofibrous aerogels are soft but flexible and effectively avoid point-to-point contact between secondary particles. [24] Those synthesized using nanoscale fibers have demonstrated good deformability with a high degree of freedom of motion. [25,26] An et al. [6] reported the fabrication of a recoverable flexible aerogel with an anisotropic layered structure via in situ crosslinking that provided excellent mechanical flexibility.

Lightweight aerogels with a high surface area, low density, and interconnected pores can be ideal for the adsorption of pollutants from industrial wastewater. [27–30] Resorcinol-formaldehyde (RF) aerogels have been recognized as good adsorbents for heavy metal ion (HMI) adsorption due to their outstanding adsorption properties. [31,32] Various strategies, such as amine modification and forming composite between graphene and Si aerogels, have been used to improve the adsorption properties of RF aerogels. [33–38] Recently, RF aerogels have been combined with other metal-based aerogels and nanofibers to improve their functionality. [39–41] Although composite RFSi aerogels research has gained much impetus due to the exceptional adsorption properties and high functionality of Si, most of them are either hard or flexible. [37,42] Hence, there is a need to produce RF-Si-crosslinked aerogels that are both rigid and flexible, thereby providing multifunctionality.

Conventional epoxy–silica hybrid aerogels typically rely on post-gelation epoxy crosslinking or surface grafting reactions, which often yield brittle networks with limited mechanical compliance [43–45]. In contrast, the present work introduces an in situ-catalyzed epoxy–thiol polymerization approach that promotes simultaneous neck formation and interparticle crosslinking during gelation. This reaction pathway generates thick, covalently reinforced silica necks that bridge adjacent particles, thereby combining high stiffness with exceptional flexibility. Unlike previously reported epoxy–silica systems, where organic domains mainly coat or bridge silica surfaces, our method induces necking enhancement directly within the inorganic framework, yielding a more continuous and mechanically robust hybrid network [46,47]. This strategy enables the fabrication of strong yet mechanically flexible aerogels without compromising porosity or transparency. Herein, we report the fabrication of a thick-necked RF-Si-crosslinked aerogel using epoxy-thiol polymerization that demonstrates high thermal insulation, and mechanical resilience and flexibility under compressive deformation. Reversible compressibility, ductile and tensile deformation, as well as recoverable bendability and buckling deformation were all displayed by the neck-enhanced RF-Si-crosslinked aerogel. Moreover, it exhibited a 10-fold higher load-bearing capacity under various deformation degrees than other resilient ceramic aerogels, [6,14] and it was capable of both HMI and methylene blue (MB) dye removal. Fig. 1 presents schematic illustration of the proposed structural mechanism in RF-Si aerogels. Fig. 1 (a) shows conventional RFSi aerogels with thin neck connections between silica and RF domains, leading to fragile frameworks; and Fig. 1(b) shows epoxy–thiol crosslinked RF-Si aerogels with thick neck junctions, providing enhanced crosslinking density, improved mechanical stability, and better resistance to pore collapse.

2. Experimental

2.1. Materials

Resorcinol (ACS reagent, 99 %), Formaldehyde solution (ACS reagent, 37 % in H_2O), GPTMS ($C_9H_{20}O_5Si$; 98 %) and MPTMS (HS$(CH_2)_3Si(OCH_3)_3$; 95 %) were purchased from Sigma–Aldrich, South Korea. Solvents such as ethanol (EtOH), and isopropanol (IPA), were obtained from Duksan chemicals (South Korea). Double distilled (DI) water was used in all the synthesis experiments. All chemicals were used as received without further purification.

2.2. Synthesis of RFSi-crosslinked aerogels

Both in situ epoxy-thiol polymerization and a sol-gel process were used to synthesize RFSi-crosslinked aerogels based on previous reports. [29,48] The RF and GPTMS-MPTMS ratios were fixed at 1:2 and 1:1, respectively, and the EtOH/water mixture was used as the solvent system. The RF and GPTMS-MPTMS mixtures with appropriate amounts of water and EtOH were stirred separately to obtain a homogeneous sol. The RF precursor sol was synthesized by stirring in water/EtOH solvent. Afterward, the two sols were mixed and stirred for 1 h to obtain a homogenous RF-crosslinked GPTMS-MPTMS sol via in situ crosslinking and a sol-gel reaction. The homogeneous RF/GPTMS-MPTMS sol was transferred to a glass vial that was closed tightly and kept at 60 °C to proceed gelation. Without an external catalyst, gelation took around 3 h; water present in the sol induced hydrolysis and condensation, whereby an RF-Si-crosslinked alcogel was obtained. After aging and a solvent exchange process, ESCD under an N_2 atmosphere was used to extract the EtOH and obtain S-RFGM_SCD aerogels or APD was used to obtain S-RFGM_APD xerogels. For comparison with the S-RFGM-based aerogels, N-functionalized RF/SiO_2 (N-RFSi_SCD) was synthesized by using a previously reported method. [49] The N-RFSi_SCD was used for comparison with present aerogels. We used two different alcohols (EtOH or IPA) with water; the details of the optimization data for EtOH/water and IPA/water solvent systems can be found in the Supporting Information.

2.3. Characterizations

Several characterization techniques were used to examine the morphological, structural, physical, and mechanical properties of the produced aerogels. To examine their chemical structures, FTIR spectroscopy was carried out at wavelengths from 400 to 4000 cm^{-1} using a PerkinElmer 1760× spectrophotometer. TGA was conducted on an SDT 2960 instrument (TA Instruments, USA) at a heating rate of 10 °C/min to determine their decomposition temperatures. Field emission SEM (JSM-7001F, JEOL, Japan) was used to image their microstructures. N_2

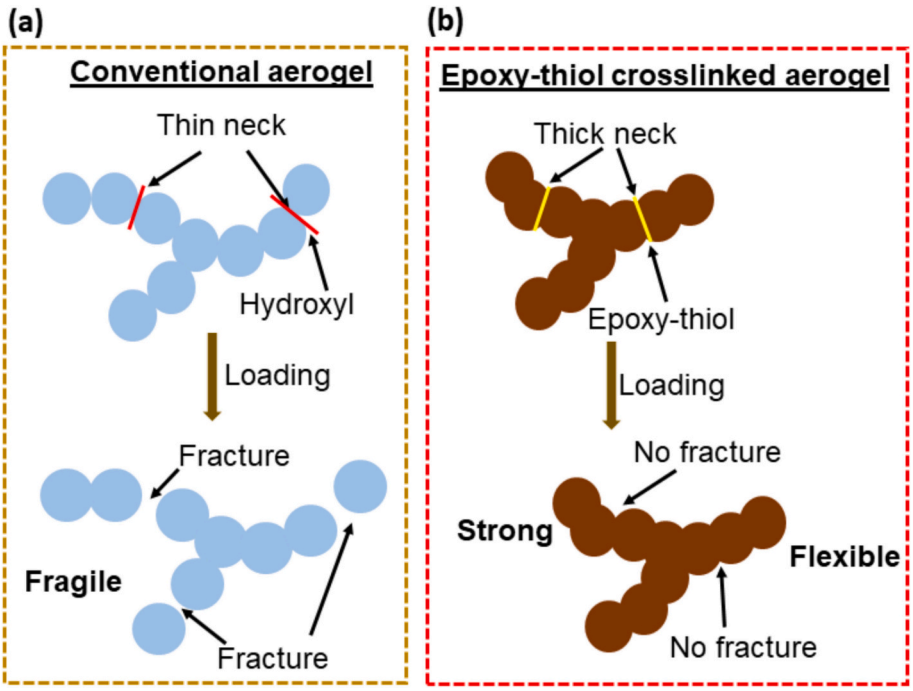

Fig. 1. Schematic mechanism of (a) conventional thin neck fragile aerogel and (b) epoxy-thiol crosslinked thick neck strong yet flexible aerogel.

adsorption-desorption isotherm data were obtained using a surface area analyzer and Quantachrome Instruments v10.0 was utilized to compute the surface area, pore volume, and pore size of the aerogels by utilizing the Brunauer–Emmett–Teller (BET) and Barett–Joyner–Halenda (BJH) techniques. To study the surface electronic states of the aerogels, XPS was performed using a monochromatic Al X-ray source (Al Kα line: 1486.6 eV, 3 mA, and 12 kV) and a K-alpha spectrometer (Thermo VG, UK). Uniaxial compression testing was performed on the prepared aerogels to evaluate their mechanical characteristics (out—05D, Oriental TM Corp., Korea). The details regarding batch adsorption experiments are provided in Supplementary Sections S1–S3.

3. Results and discussion

3.1. Synthesis and physical properties of RF-Si aerogels

It is necessary to adopt a suitable crosslinker and Si precursor to provide robust monolithic RF-Si aerogels with a high elastic modulus value. A facile in situ epoxy-thiol polymerization and sol-gel process was used to produce a thick-necked microstructure therein. Fig. 2 presents a schematic for the synthesis of an S-RFSi_SCD aerogel using an ethanol (EtOH) supercritical drying (ESCD) process. Meanwhile, Fig. S1 illustrates the formation mechanism for the RFSi-crosslinked aerogels using the in-situ crosslinking method. First, Si precursors 3-glycidyloxypropyltrimethoxysilane (GPTMS; $C_9H_{20}O_5Si$) and MPTMS ((3-mercaptopropyl) trimethoxysilane; $HS(CH_2)_3Si(OCH_3)_3$) were dissolved in a solvent mixture of water/EtOH, as were resorcinol and formaldehyde in a separate solution. After 1 h, both solutions were mixed and stirred for 1 h. The epoxy-thiol groups present in GPTMS and MPTMS proceeded the polymerization, and at the same time, resorcinol and formaldehyde underwent hydrolysis and condensation. The RFSi aerogels were obtained after drying the aged gels via ESCD. The obtained RFSi aerogels were not only mechanically strong but also flexible, making them an interesting material for various applications where both properties are

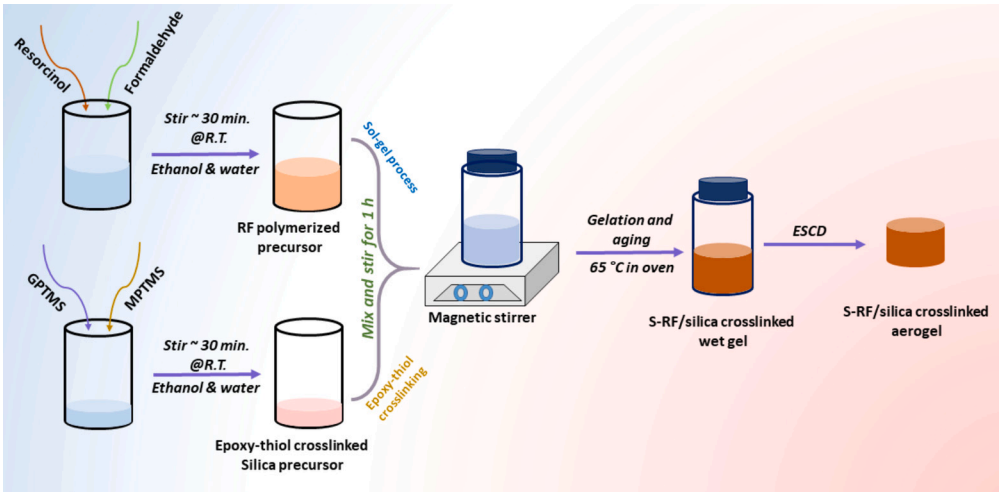

Fig. 2. A schematic presentation of the synthesis of S-RFSi aerogels using ESCD.

necessary in one material. The visible appearance of S-RFSi_SCD can be clearly observed in the images in Fig. S2.

The physical and textural properties of the RFSi aerogels prepared in EtOH/Water and isopropyl alcohol (IPA) /water solvent systems are provided in Table S1. The bulk density values for the S-RFSi_SCD, S-RFSi_APD (prepared by using ambient pressure drying (APD)), and N-functionalized RF/silicon dioxide (SiO_2) (N-RFSi_SCD; prepared by using SCD) aerogels reported in Table 1 were 0.050, 0.704, and 0.035 g/cm^3, respectively. In addition, their porosity values calculated using Eq. (1) were 96.10 %, 60.43 %, and 98.89 %, respectively, which are consistent with their bulk density values. It was found that S-RFSi_SCD had a higher density and a lower porosity than N-RFSi_SCD prepared via the traditional method. Moreover, the handling of the latter was difficult due to its soft and fragile nature. Although the bulk density and porosity values of S-RFSi_SCD and S-RFSi_APD were similar, the latter is more convenient for industrial applications. The thermal conductivity of S-RFSi_ SCD was around 0.026 W.m^{-1} K^{-1}, which is lower than other flexible aerogels. [6,50,51] This thermal conductivity value is comparable to that of still air at ambient temperature and pressure conditions. About half of this value (~0.012 W.m^{-1} K^{-1}) can be achieved in conventional silica aerogels with optimized low thermal conductivity, indicating that the sick-neck morphology increases the thermal conduction contribution due to the solid aerogel's nanoparticle network [52]. Furthermore, the solid content and morphology of nanoparticle networks can be optimized for desired simultaneous thermal insulation and mechanical properties.

3.2. FTIR, TGA, and XPS analysis results

The double crosslinking approach with the sol-gel process impacted the physical, morphological, and mechanical properties of the RFSi aerogels but not the chemical bonding within them. FTIR spectra for the S-RFSi_APD, S-RFSi_SCD, and N-RFSi_SCD aerogels are presented in Fig. 3(a). In addition, FTIR spectra for S-functionalized RF/GPTMS-MPTMS aerogels synthesized in EtOH/water (S-RFGME) and IPA/water (S-RFGMI) solvent systems are presented in Fig. S3. The FTIR spectra in Fig. 3(a) show similar stretching and bending vibrations, except for C—O bond vibration at 1287 cm^{-1}, [39] and the Si—O and Si—C peaks observed at 1080 and 1455 cm^{-1}, respectively, indicating the formation of RFSi-crosslinked aerogels. [39] C—H vibrations were confirmed by peaks appearing at 1455 and 2926 cm^{-1}. [40] The hydrophilic character of the produced RFSi aerogels was confirmed by the presence of O—H groups at 1614 and 3341 cm^{-1}. [53] Moreover, GPTMS and MPTMS crosslinking was confirmed by peaks at 1721, 904, and 697 cm^{-1} assigned to C═O, C—S, and S—O, respectively. [39] The FTIR results indicate that epoxy-thiol crosslinking and the sol-gel procedure were responsible for the formation of the double-crosslinked RF-Si aerogels.

Fig. 3(b) shows TGA thermograms for S-RFSi_APD, S-RFSi_SCD, and N-RFSi_SCD under airflow. In addition, the TGA profiles for S_RFSi aerogels optimized using EtOH/water and IPA/water solvent systems are provided in Fig. S4, and the decomposition temperature and weight loss at 300 °C and 800 °C are reported in Table S2. All of the samples showed 4–7 % weight loss at 300 °C under N_2 and air atmospheres. However, the weight loss at 800 °C under both atmospheres was around 40 % and 80 %, respectively. This indicates that the char yield due to the carbonization of RF in the presence of Si under an N_2 atmosphere was around 60 %, while that under an oxygen atmosphere was ~20 %, representing the Si in the RF-Si aerogels. [54] The thermograms in Fig. 3 (b) indicate that the S-RFSi_SCD and N-RFSi_SCD samples decomposed in one step from 284 to 627 °C and 284 to 693 °C, respectively. However, the decomposition of the S-RFSi_APD sample was in two steps: 100 to 235 °C and 235 to 627 °C. Moreover, 16.17 %, 20.15 %, and 40.33 % of thermally stable char residue were formed after the decomposition of S-RFSi_APD, S-RFSi_SCD, and N-RFSi_SCD, respectively. The TGA analysis results reveal that the RF polymer completely decomposed under an air atmosphere and the residual weight corresponded to the presence of Si after decomposition of the samples. Thus, the three samples show good thermal stability due to Si-crosslinking. The N-RFSi_SCD sample with an Si network of higher than 40 % showed good thermal stability, which was due to the higher amounts of Si precursors used during its synthesis.

The N_2 adsorption-desorption isotherms and pore-size distributions obtained using the BJH method are displayed in Fig. 3(c) and 3(d), respectively. The calculated BET specific surface areas for the S-RFSi_APD, S-RFSi_SCD, and N-RFSi_SCD samples were 185.2, 307.2, and 391.5 m^2 g^{-1}, respectively. The S-RFSi_APD sample contained only *meso*pores with an average BJH pore diameter of ~13 nm. However, S-RFSi_SCD contained micro-, meso-, and macropores with an average pore diameter of 15.62 nm while N-RFSi_SCD contained many micropores with an average pore size of 1.53 nm. Moreover, S-RFSi_SCD had a lower specific surface area than N-RFSi_SCD, likely due to the two Si co-precursors (GPTMS and MPTMS) used in the synthesis of the former. The average pore volumes determined by using the BJH approach and N_2 can only be used to identify microporous and mesoporous structures: the average pore volumes for S-RFSi_APD (meso), S-RFSi_SCD (micro and meso), and N-RFSi_SCD (micro and meso) were 0.606, 1.200, and 2.664 cm^3/g, respectively (Fig. 3(b)).

3.3. Morphological and BET surface area analyses

SEM images of the S-RFSi_APD, S-RFSi_SCD, and N-RFSi_SCD samples shows that they contain highly porous 3D networks. The SEM image of the S-RFSi_APD in Fig. 4(a) reveals the aggregation of dense colloidal RF-Si-crosslinked particles linked together, which is consistent with the density and porosity measurements (Table 1). The highly porous 3D networks in both the S-RFSi_SCD and N-RFSi_SCD samples contained fibril-like connections between the RF-Si colloidal particles tens of nanometers in size (Fig. 4(b) and 4(c)). The S-RFSi_SCD sample contained a few micropores and macropores, and many mesopores (Fig. 4 (b)). However, the N-RFSi_SCD sample contained more micropores than mesopores and/or macropores, along with agglomeration in some parts. Thus, the hierarchical porous network in S-RFSi_SCD can be effectively used in versatile applications. In addition, the SEM morphologies for S_RFSi aerogels synthesized using the EtOH/water and IPA/water solvent systems are provided in Fig. S5. The SEM results are consistent with the BET surface area and BJH pore-size distribution measurements. Microstructural differences between the S-RFSi_APD, S-RFSi_SCD, and N-RFSi_SCD samples were clarified by using TEM. The TEM images in Fig. 4(d) and 4(e) reveal that the S-RFSi_APD sample showed

Table 1
Physical and textural properties of the RF-Si-crosslinked aerogels.

Sample	Bulk density (g. cm^{-3})	Skeletal density (g.cm^{-3})	Porosity (%)	BET surface area (m^2. g^{-1})	Pore volume (cm^3. g^{-1})	Average Pore diameter (nm)	Thermal conductivity (W·m^{-1} K^{-1})
S-RFSi_APD	0.704	1.78	60.43	185.2	0.606	13.09	0.050
S-RFSi_SCD	0.050	1.28	96.10	307.2	1.200	15.62	0.026
N-RFSi_SCD	0.035	3.17	98.89	391.5	2.664	1.53	0.025

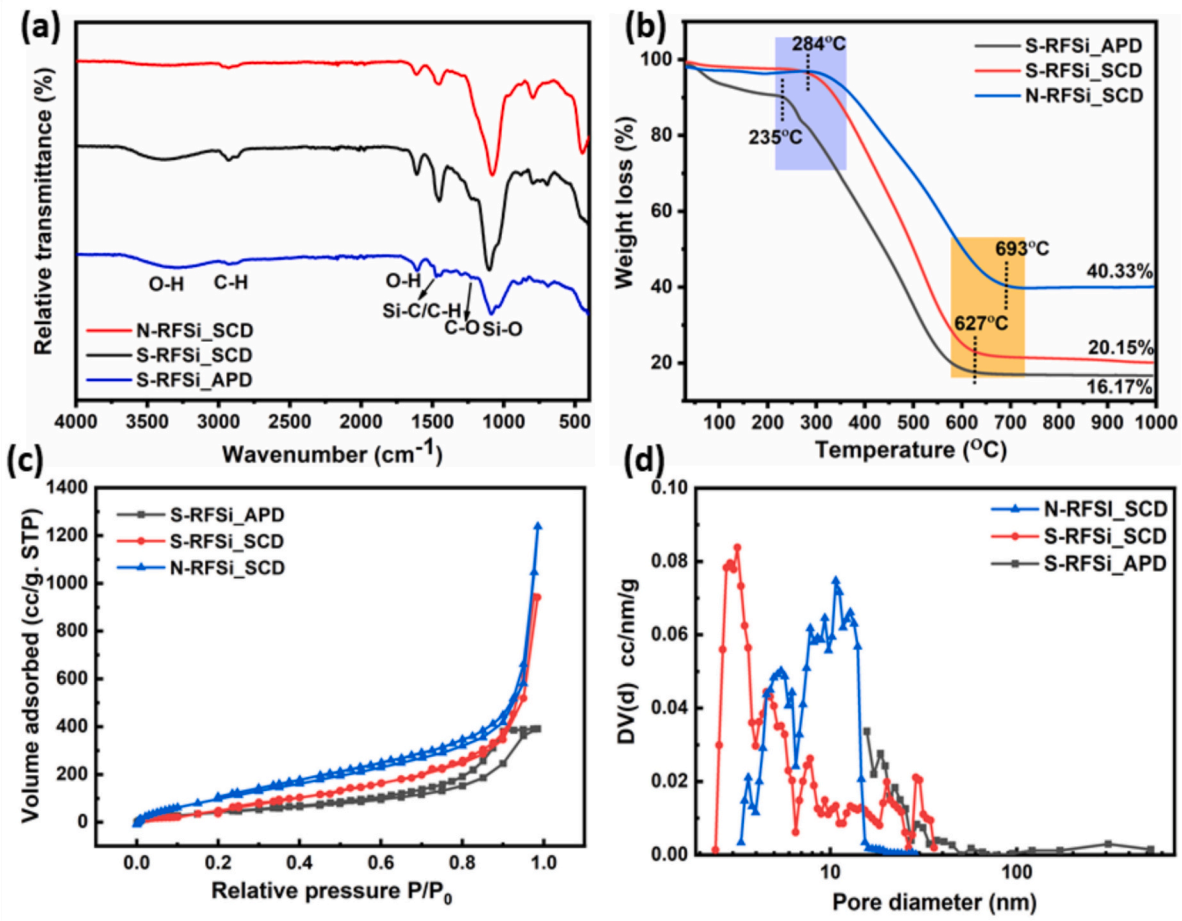

Fig. 3. (a) FTIR spectra, (b) TGA profiles, (c) N_2 adsorption-desorption profiles and (d) BJH pore volume data for the S-RFSi_SCD, S-RFSi_APD, and N-RFSi_SCD aerogels.

agglomeration and S-RFSi_SCD contains many mesopores (Fig. 4(d)) whereas the N-RFSi_SCD sample had more meso- and micropores (Fig. 4 (e)).

Fig. 4 (g-i) provides high-resolution TEM images for S-RFSi_APD, S-RFSi_SCD, and N-RFSi_SCD; S-RFSi_APD contained agglomerates of RF-Si nanoparticles with thick necking, which agrees with its physical and morphological properties (Fig. 4(i)). N-RFSi_SCD contained thin and disordered necking with a thickness of 27.8 ± 2.1 nm and a length of 34 nm (Fig. 4(i)); there were no distinguishable connections in the two necking regions, which makes it softer and is consistent with the density and porosity values. However, S-RFSi_SCD displayed thick and ordered necking with an average thickness of 41.7 ± 3.2 nm and a length of 83.4 nm (Fig. 4(h)); these improvements in necking thickness and length are due to the epoxy-thiol polymerized GPTMS and MPTMS chains and crosslinking by the RF polymer.

The gelation time for the S-RFSi_SCD aerogel was slower than that of the N-RFSi_SCD aerogel (~3 h vs. ~1 h), which could have helped strengthen the network via necking enhancement. [18,55] In fact, the increases in the length and thickness of the necking region comprising a semi-fibril network could have improved the strength and mechanical flexibility of the aerogel. [56,57] Moreover, the predominant addition reactions could have increased the connection points in the network with thick necking.

The EDS elemental mapping data for S-RFSi_SCD, S-RFSi_APD, and N-RFSi_SCD samples in Figs. S6, S7, and S8, respectively, confirmed that S-RFSi_SCD and S-RFSi_APD contained C, O, Si, and S whereas N-RFSi_SCD contained C, O, Si, and N. All of the elements were uniformly distributed, thereby confirming the strong crosslinking in the Si and polymerized RF network.

3.4. Mechanical properties

The mechanical performances of the prepared S-RFSi_SCD, S-RFSi_APD, and N-RFSi_SCD samples were measured using a universal test machine (UTM); their compressive stress-strain curves at a loading rate of 0.5 mm min^{-1} are presented in Fig. 5(a). The differences in compressive stress–strain behavior among S-RFSi_SCD, S-RFSi_APD, and N-RFSi_SCD are likely related mainly to the geometry of their necking regions, which control stress distribution and deformation capacity. In S-RFSi_SCD, the necks are both thick and relatively long, providing a large load-bearing area to enhance compressive modulus and maximum stress while allowing bending and deflection for good flexibility, resulting in a strong yet ductile response. In contrast, S-RFSi_APD possesses thick but short necks, which efficiently resist stress and yield high modulus and maximum stress but limit strain accommodation, leading to a stronger but more brittle structure. By comparison, N-RFSi_SCD has thin necks that act as stress concentrators, promoting early buckling or fracture and producing low compressive modulus and maximum stress, making it mechanically the weakest. Fig. 5(b) illustrates that the S-RFSi_SCD aerogel exhibited strong reversible compressibility as it could rebound to almost its original size after being squeezed by 10 % to 50 % strain, as has been reported for several lightweight ceramic aerogels. [18,19,58,59] The compressive modulus and maximum stress for S-RFSi-SCD aerogel calculated from the initial linear stage are approximately 5.65 and 1.8 MPa, respectively.

The S-RFSi_SCD aerogel showed high fatigue resistance under

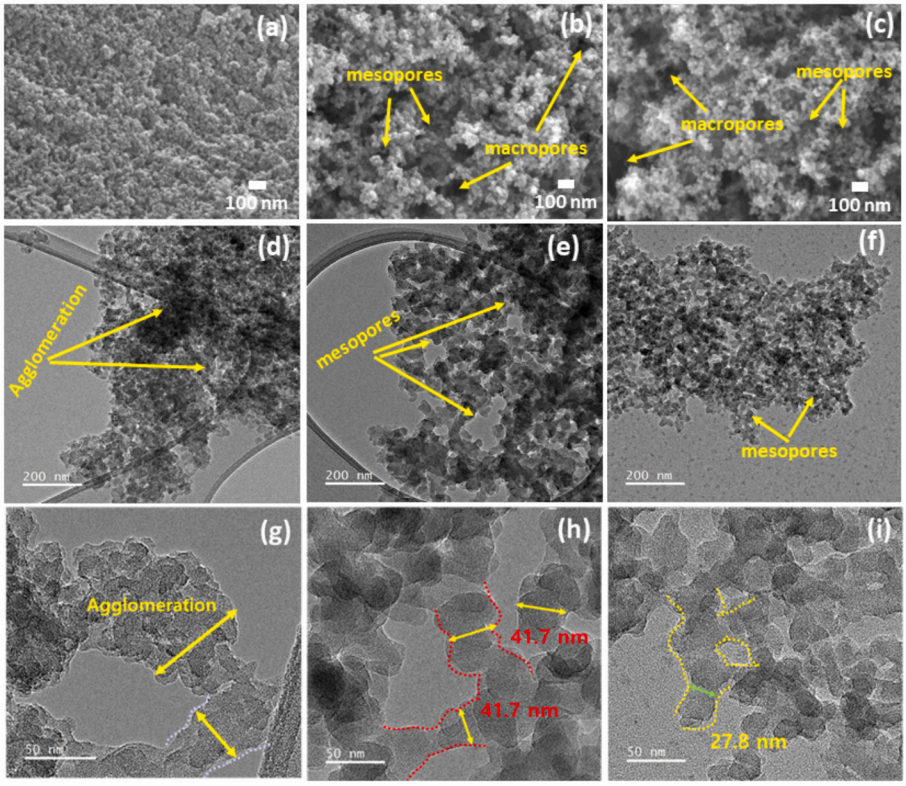

Fig. 4. (a–c) SEM and (d-f) TEM images of S-RFSi_APD, S-RFSi_SCD, and N-RFSi_SCD aerogels. Meso-, and macropores are indicated by the arrows. TEM images of the necking connections in the (g) S-RFSi_APD, (h) S-RFSi_SCD, and (i) N-RFSi_SCD aerogels. The neck regions are indicated by yellow and red dotted lines.

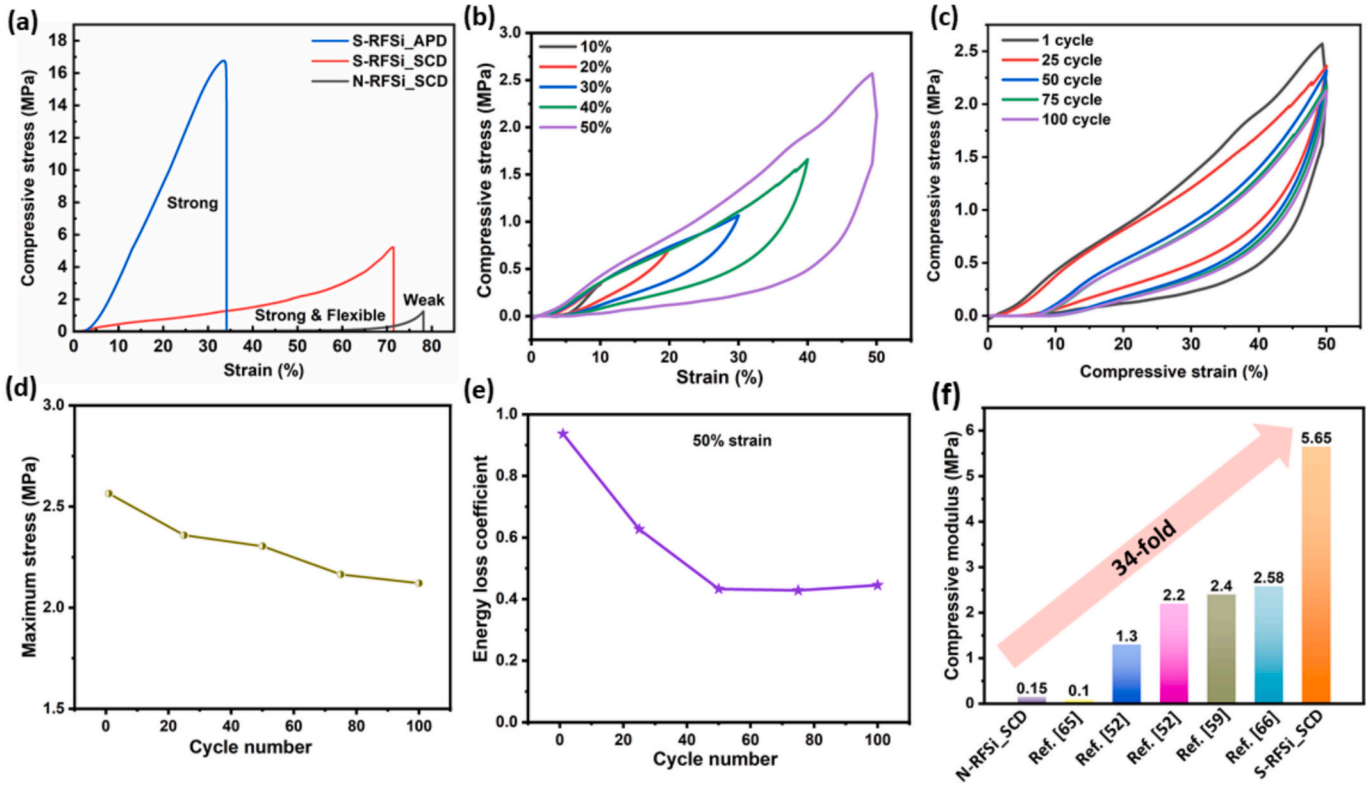

Fig. 5. (a) Compressive stress-strain curves for the S-RFSi_APD, S-RFSi_SCD, N-RFSi_SCD aerogels. Investigation of other mechanical properties of the S-RFSi_SCD aerogel: (b) consecutive compressive stress-strain curves from 10 % to 50 % strain, (c) cyclic compressive fatigue testing under 50 % constant strain, (d) maximum compressive stress during 100 fatigue cyclic tests (e) maximum energy loss coefficient during 100 fatigue cyclic tests, and (f) comparison with the reported compressive modulus values for other hybrid RFSi-based aerogels.

compression. The stress-strain curves of the aerogel during 100-cycle fatigue tests at a fixed strain of 50 % are displayed in Fig. 5(c); there was no lasting deformation within the first 25 cycles while persistent strain of around 7 % was observed after 50 cycles and same behaviour observed for maximum stress (Fig. 5(d)). The S-RFSi_SCD aerogel displayed a high mechanical energy loss coefficient of 0.9 in the first cycle of loading and unloading, which then remained constant at around 0.4 after 50 cycles (Fig. 5(e)). This suggests effective mechanical energy dissipation and thus good mechanical impact resistance. The compressive modulus value for S-RFSi_SCD is better than those reported for other RF-Si composite aerogels. We found that traditional (3-aminopropyl) triethoxysilane (APTES)-catalyzed hybrid RFSi aerogels attained a compressive modulus of 0.15 MPa (Fig. 5(f)), which is 34-fold lower than S-RFSi_SCD. Thus, there are differences between the mechanical properties of S-RFSi_SCD and previously reported RF-silicon dioxide (SiO_2) aerogels, [42,54,60–62] with the former showing higher stiffness and load-bearing capacity (supplementary table S3). The improved mechanical properties of the S-RFSi_SCD aerogel are due to the necking thickness enhancement. Images of the compression and recovery process for S-RFSi_SCD are presented in Fig. S9 while the possible changes therein during uniaxial compression are presented in Fig. S10. These results prove that the mechanical flexibility and strength of S-RFSi_SCD are due to the epoxy-thiol polymer network and RFSi network.

The S-RFSi_SCD sample shows better mechanical properties than the S-RFSi_APD and N-RFSi_SCD samples due to having longer and thicker necking. Wu et al. [63] reported a phenolic aerogel with a thick united nanostructure and excellent mechanical strength, supported by conducting a finite element analysis (FEA). Unlike the pearl necklace-like network in typical RF aerogels, that in our hybrid RFSi aerogel comprises long and thick necks. In general, connected necks can be generated via condensation of an organic precursor and grown by the dissolution-reprecipitation of polymer agglomerates during aging of the gel. In the present study, the creation of a thick-necked network with long necking connections was aided by the slow polymerization of RF and GPTMS-MPTMS in a double-distilled (DD) water and EtOH mixture, which further provided mechanical strength as well as flexibility.

3.5. Neck dimensions of RFSi aerogels

It has been reported that the aerogels derived from a high RF concentration are physically stiffer whereas ones derived from a higher Si precursor concentration are softer. [47,63] In the present work, N-RFSi_SCD contained lower concentrations of RF and APTES than GPTMS and MPTMS in S-RFSi_SCD. Hence, as seen in the TEM images, the network in N-RFSi_SCD was more disordered than that in S-RFSi_SCD with long thick necking. It has long been known in sol-gel science that during the aging process, regions with high curvature (i.e., the concave topography defining the necks between two covalently bonded nanoparticles) are susceptible to selective precipitation. [64,65] This thickens the region and increases the post-gelation strength of the networked porous solid. The necking enhancement was consistent with the growth of the N-RFSi_SCD and S-RFSi_SCD aerogels in that region, which provided them with better mechanical strength while retaining flexibility.

The mechanical properties of aerogels are significanty influenced by morphology and pore connectivity. The three distinct phenomena were observed in the prepared RFSi aerogels with changing crosslinking parameters and drying method. The schematic presentation for necking dimensions of N-RFSi_SCD, S-RFSi_APD, S-RFSi_SCD, aerogels have been provided in Fig. S11. According to necking arrangements in TEM (Fig. 4), the obtained aerogels possess thin and disordered necking (N-RFSi_SCD), thick and ordered necking (S-RFSi_SCD), and thick and agglomerated necking (S-RFSi_APD). The N-RFSi_SCD aerogels consists low density, high porosity with weak and sparse necking connections, resulting in the lack of uneven stress distribution. This weak necking arrnagments resulted in poor mechanical strength and brittle behavior. The S-RFSi_APD aerogel irregular necking with agglomerated particles, increasing the mechanical strength of aerogels. However, S-RFSi_SCD aerogel withstands at mechanical stress due to thick and ordered neck arrangements, leading to mechanically strong yet flexible nature.

4. Finite element analysis

4.1. The FEA model

FEA simulations were carried out to better understand the properties of the S-RFSi_SCD aerogel. A representative section of the aerogel shown in Fig. 6(a) was reproduced to understand how the compressive properties of the aerogel are affected by the neck radius (n) and interparticle chemical reaction area (d). The mechanical properties of aerogel pore walls differed significantly in string-of-pearls and a constant cross-section model. This is because the former, which more accurately reflects the structure of aerogels, introduces variations in the cross-section of the pore walls, specifically at the interparticle necks. The unit cell had an RF/Si particle radius of 22.5 nm. The Young's modulus of the RF/Si nanoparticles was 70 GPa with a Poisson ratio of 0.19, while those for the epoxy-thiol crosslinking reaction were 0.5 GPa and 0.3, respectively. The system was composed of 3 nanoparticles and two epoxy-thiol reaction areas (Fig. 6(b)). The FEA model was used to study the buckling behavior of pore walls designed with varying neck sizes started by varying their radius (p) from 5 to 100 nm (Fig. 6(b)). The distance between the Si particles (d) was varied from 0.5 to 7.5 nm.

The buckling analysis was performed using ANSYS Parametric Design Language (APDL). Boundary conditions were applied to fix all degrees of freedom at one end of the RF/Si nanoparticle, while a compressive force was applied at the other end. First, a static analysis was conducted to establish the initial stress state under the applied load. This was followed by a linear perturbation buckling analysis to determine the critical buckling load and the corresponding mode shapes. The buckling analysis involved restarting the static analysis and performing a perturbation analysis to solve for the buckling modes. The results of the analysis included the critical buckling load, which indicates the load at which 3 RF/Si nanoparticles are expected to buckle, and the mode shapes, which show the deformation pattern of the beam at buckling. In addition, the maximum displacement at the node with the highest value was used to calculate the strain in the applied load region. The effect of fillet radius on the Von Mises stress is provided in Fig. 6 (c), resulting in the increase of neck region can enhances the applied stress.

4.2. Influence of neck size on critical buckling load

Simulations were carried out by varying the neck radius while keeping the distance between the RF/Si nanoparticles constant. The results show that as the neck size increased in a pearl-necklace-like pore wall, the critical buckling load also increased as shown in supplementary Fig. S12. This relationship is due to the impact of neck size on stress concentration and the overall stability of the pore wall. When the necks between the particles are small, they act as stress concentrators, meaning that the stress at these points is significantly higher than in the surrounding material. This higher stress concentration makes the pore wall more susceptible to buckling at lower loads. As the neck size increased, the stress concentration effect diminished. This is because a larger contact area between the particles enabled a more even distribution of stress, thereby increasing the pore wall's resistance to buckling. As the neck size approaches the particle radius, the pore wall essentially behaves like a continuous beam with a constant cross-section. Analyzing the compressive strain defined as displacement at the load location divided by the overall length of the 3-particle system, it can be observed that as the neck radius increased (as a function of p), the strain increased. This is because more flexibility is provided by the epoxy-thiol crosslinking reaction and a small radius enables the RF/Si nanoparticles to be in contact with each other, thereby reducing the

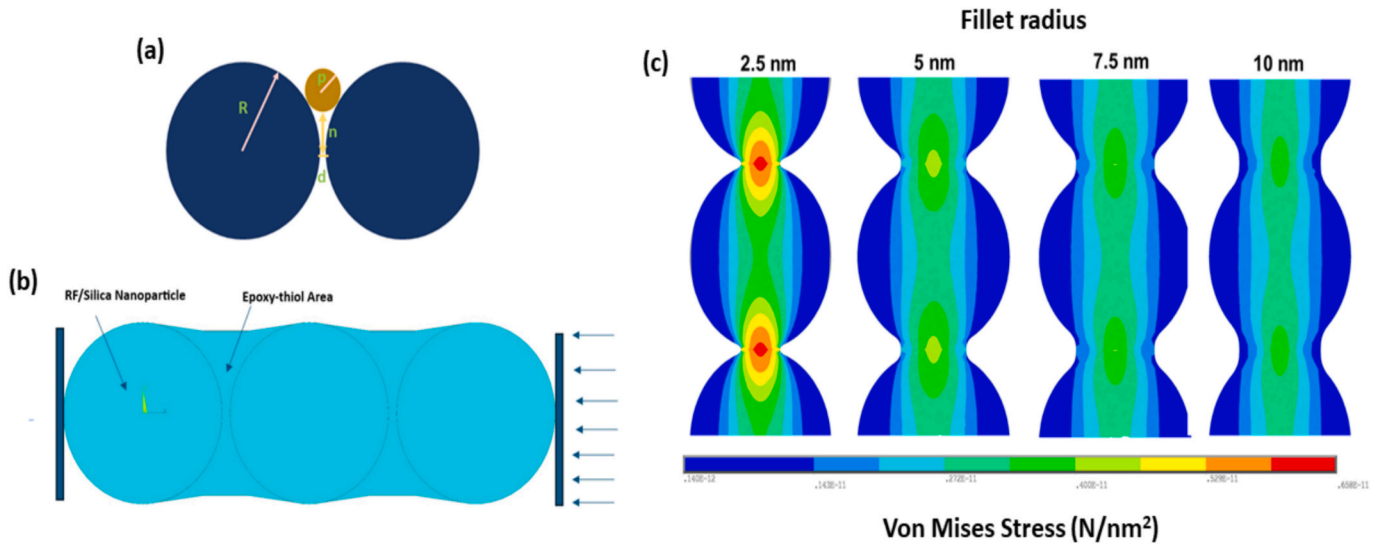

Fig. 6. FEA simulation results for the S-RFSi_SCD aerogel: (a) a three-particle system modeled under compressive loading and (b) a three-RF-Si nanoparticle system within the epoxy/thiol neck area under compressive loading, and (c) Von Mises Stress as a function of Fillet radius.

maximum strain.

4.3. *Influence of interparticle distance on the critical buckling load*

The modeling was also carried out for a constant neck radius while varying the gap between the RF/Si nanoparticles to simulate the epoxy-thiol crosslinking reaction presented in supplementary Fig. S13. The results show that as the gap was increased, there was a nonlinear relationship between the gap of the buckling load. Similar behavior was experienced under normalized strain: the higher the gap between the nanoparticles, the lower the buckling load or the maximum strain. When the gap between the particles is small, fewer epoxy-thiol crosslinks are present, meaning that the load is mainly absorbed by the RF/Si nanoparticles and the buckling load is significantly higher when more epoxy-thiol crosslinks are present. The gap acts as a softening mechanism that makes the pore wall more susceptible to buckling at lower loads or adding more ductility to the aerogel. This analysis offers a potential explanation for the properties observed in the manufactured S-RFSi_SCD aerogel.

The TEM-measured neck diameter (41.7 nm, radius ≈ 20.9 nm) lies within the simulated neck radius range (5–100 nm), confirming that the model parameters are representative of the experimental system. Supplementary Fig. S14 shows a clear positive correlation between neck radius and compressive modulus. Specifically, the S-RFSi_SCD sample, with a neck thickness of ~41.7 nm, exhibited the highest compressive modulus (5.65 MPa), whereas samples with smaller neck radii showed proportionally lower moduli. The neck enhancement is governed by the epoxy–thiol crosslinking density and the MPTMS/epoxy precursor ratio. Increasing thiol content promotes localized polymer growth at particle junctions, leading to thicker necks and enhanced load transfer efficiency.

5. Water-treatment applications

5.1. *Mercury (Hg^{2+}) removal*

The developed S-RFSi aerogel's capacity to adsorb HMIs was systematically evaluated. The pH value is critical to the adsorption of HMIs because it affects both the degree of ionization of HMIs and the adsorbate's capacity to adsorb them. To determine the optimized pH value, the zeta potential was measured at different pH values (3−12), the outcome of which is presented in Fig. 7(a). At the highest pH of 12, the aerogel had a low negative zeta potential because the thiol groups therein produced negative surface charges. The comparative analysis for

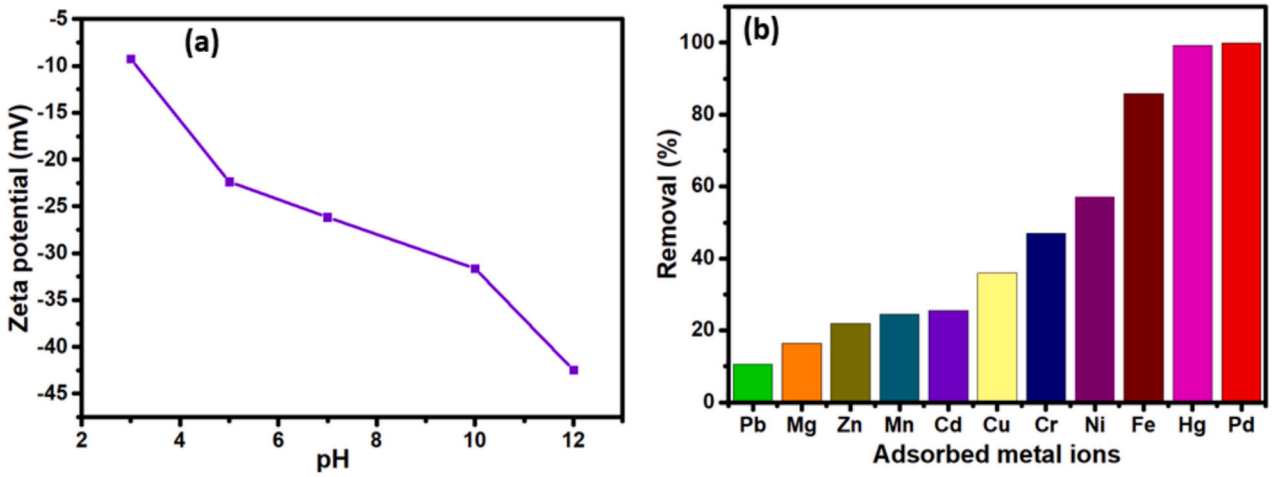

Fig. 7. (a) Zeta potentials at various pH values and (b) the removal of various HMIs by the S-RFSi_SCD aerogel at ambient temperature.

Hg removal by S-RFSi_SCD, S-RFSi_APD, and N-RFSi_SCD aerogels is provided in supplementary Fig. S15. The S-RFSi_SCD aerogel shows higher Hg adsorption than S-RFSi-APD and N-RFSI_SCD aerogels. Furthermore, the removal percentages for various HMIs by the S-RFSi aerogels are shown in Fig. 7(b); it was found that the S-RFSi aerogel could adsorb large amounts of Pd^{2+} and Hg^{2+} ions. Hg^{2+} is heavier than Pd^{2+}, so we concentrated on the removal study of the former. The S-RFSi_SCD sample showed very effective removal of Hg^{2+} (99 %). Several other materials, including activated carbon, thiol-functionalized Si, zeolites, and metal-organic frameworks, have been reported to be capable of selective Hg adsorption (Table 2). It is crucial to produce an adsorbent with high efficiency and selectivity for Hg removal. The S-RFSi_SCD aerogel's S-functional groups and hierarchical pores together with its excellent physical and chemical properties enable its great adsorption efficiency and selectivity for Hg^{2+} ions.

Fig. 8(a) shows the calculated percentage removal and the adsorption capacity at equilibrium (q_e) for Hg^{2+} adsorption using 10–100 mg S-RFSi_SCD adsorbent. The starting Hg^{2+} ion concentration and pH for this experiment were 100 mg/L and 7, respectively. As the dose of the adsorbent was increased from 5 to 25 mg, a steady drop in Hg^{2+} adsorption efficiency was observed, ranging from 970.28 to 198.76 mg/g. The observed decrease in adsorption capacity per unit mass (q_e) with increasing adsorbent dose primarily reflects an equilibrium/mass-balance effect rather than loss of intrinsic adsorption activity. A mass-balance calculation in supplementary section S4 shows that the absolute mass of Hg removed is essentially constant (≈4.85 mg for 5 mg adsorbent and ≈4.97 mg for 25 mg adsorbent); increasing the adsorbent mass therefore reduces q_e because the same quantity of Hg is shared over more adsorbent. Nevertheless, physico-chemical factors such as particle aggregation at higher solid loadings which can reduce accessible surface area and pore accessibility may further reduce the effective uptake per gram.

In addition, utilizing 5 mg of aerogel adsorbent resulted in the maximum adsorption capability for Hg^{2+} (970.28 mg/g) (Fig. 8 (a)). Therefore, 5 mg of S-RFSi_SCD aerogel adsorbent was the optimal dose for maximizing the removal of Hg^{2+}. One way to determine the concentration of cationic metal species is to measure the pH of the solution. The impact of changing the pH level on Hg^{2+} adsorption can be seen in Fig. 8(b). In addition, pH = ~6 (considered as standard for determining the adsorption capacity for Hg^{2+} ions) provided the maximum Hg^{2+} adsorption capability of ~990 mg/g. The adsorption of HMIs can vary at different pH values because the surface hydroxyl and thiol functional groups on the aerogel surface undergo fast protonation and deprotonation at low and high pH, respectively. It was also confirmed that equilibrium was reached in the adsorption process for metal ions after 30 min. Thus, a set contact time of 30 min was used for subsequent experiments, the results of which are shown in Fig. 8(c).

To clarify the adsorption process for the S-RFSi_SCD aerogel, Fig. 8 (d) and 8(e) show fitted graphs for nonlinear pseudo-first-order and linear pseudo-second-order kinetic models for Hg^{2+} adsorption by the aerogel, respectively, the experimental data for which are reported in Table S4. The nonlinear pseudo-first-order fitting and second-order linear fitting curves yielded coefficient of determination (R^2) values of ~0.8 and ~ 1, respectively, with an adsorption capacity of 1000 mg/g. This indicates that the adsorption of Hg^{2+} ions by the S-RFSi_SCD aerogel involves pseudo-second-order kinetics, thereby suggesting chemisorption by the thiol and hydroxyl functional groups on the aerogels and that the rate of Hg^{2+} adsorption depends on the availability of sorption sites. Fig. 8(f) shows that the q_e value varied according to the initial Hg^{2+} concentration. The results for fitting adsorption isotherms using the Langmuir and Freundlich isotherm models for Hg^{2+} are shown in Fig. 8(g) and 8(h), respectively. The pseudo-second-order model was shown to be the predominant mechanism for chemical adsorption, and the Langmuir model was fitted to determine the monolayer adsorption capacity. The maximum adsorption capability of the S-RFSi aerogel by the thiol and hydroxyl functional groups on the aerogels and that the rate of Hg^{2+} adsorption depends on the availability of sorption sites. The maximum adsorption capability of the S-RFSi aerogel adsorbent for Hg^{2+} ions calculated using the Langmuir adsorption model was ~699.3 mg/g (Table S5). In addition, the Freundlich model provided K_F, n, and R^2 values of 794.32, 0.037, and 0.94, respectively (Table S5). It was found that the Langmuir model provided a higher R^2 value (~0.984) than the Freundlich model, thereby supporting the better suitability of the former.

The adsorption capacity of the aerogel at three different temperatures (25, 35, and 50 °C) was assessed to estimate the thermodynamic parameters. The thermodynamic parameters, such as the change in the amount of free energy (ΔG°), enthalpy (ΔH°), and entropy (ΔS°), were calculated using Van't Hoff equations (Supplementary Section S3). The corresponding graphs for Hg^{2+} ions are shown in Fig. 8(i). Table S6 provides the parameter values calculated using the aforementioned equations. The Hg^{2+} ions can pass through the aerogel pores due to their faster movement at higher temperatures. Moreover, the elimination of Hg^{2+} ions is a non-spontaneous sorption process, as indicated by the positive ΔG° values. Nonetheless, when the temperature was increased, the absolute ΔG° value rose as well, thereby suggesting that physisorption was predominant. Moreover, an exothermic adsorption process is indicated by the negative ΔH° value. This resulted from a decrease in randomness at the solid/liquid contact interface during the sorption process.

Table 2
Comparison of the maximum adsorption capacities of the aerogel and MOF adsorbents for heavy metal ions.

Aerogel adsorbent	Heavy metal ions	q_m (mg/g)	Ref.
ANFs/WS_2	Pb^{2+}	617.3	[66]
PEI functionalized chitosan	Cr^{6+}	445.29	[67]
Magnetic Carbon	Pb^{2+}	210	[68]
Amino- functionalized sodium alginate	Cr^{6+}	678.67	[69]
	Cd^{2+}	464.23	
Mercapto-RF	Cu^{2+}	120.48	[70]
	Pb^{2+}	84.03	
Mercapto-RF	Hg^{2+}	169.49	[71]
APTES-RF	Pb^{2+}	150	[72]
Fe-RF	Cr^{6+}	55	[73]
Amine modified RF	Cd^{2+}	151.52	
	Hg^{2+}	158.73	[74]
	Pb^{2+}	156.25	
GM crosslinked silica	Pd^{2+}	689.65	[29]
3D-CS-ZIF-67	Pb^{2+}	5.47	[75]
Fe-MG MOF	Pb^{2+}	196	[76]
Zr MOF	Pb^{2+}	100	[77]
Fe_3O_4-ZrMOF@GSH	Hg^{2+}	431	[78]
S-RFSi	Hg^{2+}	699.30	This work

5.2. Methylene blue (MB) dye adsorption

We investigated the ability of the S-RFSi_SCD aerogel to adsorb MB dye. Fig. 9(a) shows the effect of the pH of the aqueous MB solution on the adsorption of the latter by the S-RFSi_SCD aerogel; the percentage removal and qe values increased until pH 7, followed by a slow decline as the pH was increased, thereby proving that the aerogel provided maximum MB dye adsorption in a neutral environment. Hence, this pH value was considered optimal when investigating the other parameters influencing the adsorption of MB dye molecules. Subsequently, adsorption studies for a range of adsorbent dosages were performed at a constant MB dye concentration of 10 ppm and pH 7. Fig. 9(b) illustrates that the q_e value gradually decreased with an increase in adsorbent dosage. Varying the adsorbent dosage from 10 to 100 mg lowered the q_e value for MB molecules in the solution. However, the MB molecules were strongly adsorbed by 10 mg of S-RFSi_SCD aerogel adsorbent. We suspect that the decrease in q_e value thereafter was due to particle

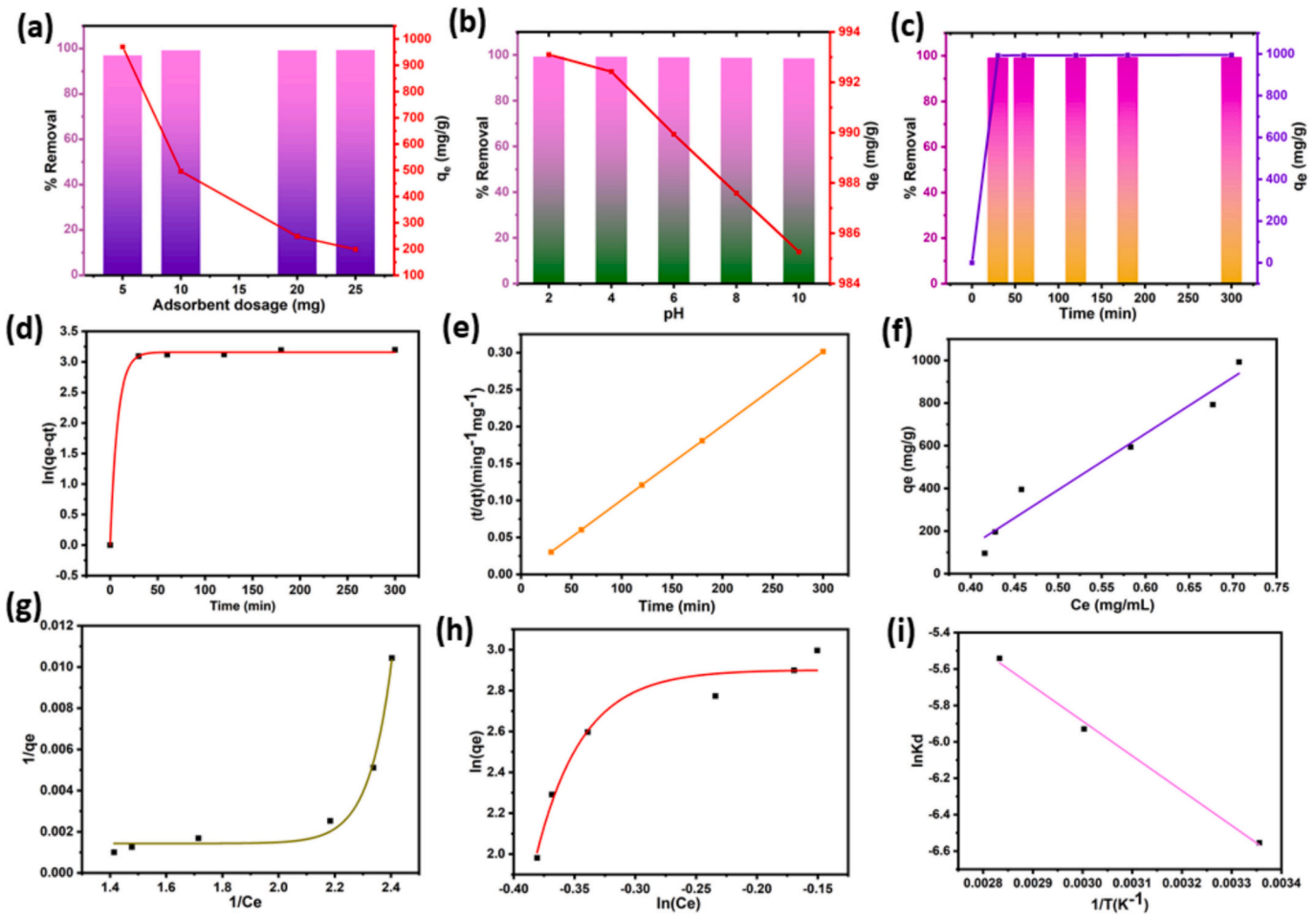

Fig. 8. (a) Effects of adsorbent dosage and (b) initial solution pH on the Hg^{2+} adsorption capacity of the S-RFSi_SCD aerogel. (c) Influence of adsorption time on the removal efficiency of Hg^{2+} by the S-RFSi_SCD aerogel. Fitted curves for the nonlinear pseudo-first-order (d) and linear pseudo-second-order (e) kinetic models. (f) Isotherm for the adsorption of Hg^{2+} on the S-RFSi_SCD aerogel's surface. (g) Nonlinear Langmuir isotherm model, (h) nonlinear Freundlich isotherm model, and (i) a Van't Hoff plot for the adsorption of Hg^{2+} by the S-RFSi_SCD aerogel.

agglomeration in the adsorbent.

The contact time between the adsorbent and the adsorbate is significantly important in wastewater treatment. The contact time for 10 ppm MB dye solution and 10 mg S-RFSi_SCD aerogel adsorbent was varied from 0 to 300 min. The adsorbent showed fast MB dye adsorption after 30 min, followed by gradual adsorption that almost reached equilibrium after 150 min (Fig. 9(c)). Hence, the latter optimal contact time was used in further MB dye adsorption experiments.

MB can easily occupy the available adsorption sites on the S-RFSi aerogel at low concentrations, which could be due to an increase in electrostatic interactions between the MB molecules and the adsorbent's empty active sites (Fig. 9(d)). In addition, due to inaccessible adsorption sites in aerogels, an increase above an initial concentration of 10 ppm may not improve the *qe* and percentage removal. When the initial MB concentration was increased from 10 to 100 ppm, the q_e of the S-RFSi_SCD adsorbent varied from 145.15 and 11.29 mg/g. This confirms that the aerogel adsorbent showed maximum MB adsorption of ~145.15 mg/g from the initial 10 ppm solution, which was due to the thiol (SH) groups on the epoxy-thiol-based aerogel surface.

The MB adsorption kinetics were investigated to understand the adsorption process and rate. Thus, both pseudo-first-order and pseudo-second-order kinetic models were investigated. Both models were indicated in the MB adsorption process by the S-RFSi_SCD adsorbent, as presented in Fig. 9(e) and 9(f), respectively, the kinetic parameter values for which are summarized in Table S7. The results show that the pseudo-second-order model correlation coefficient (0.9974) was higher than that for the pseudo-first-order model (0.93), thus pseudo-second-order kinetics control the MB adsorption by the S-RFSi aerogel adsorbent.

MB adsorption by the S-RFSi_SCD adsorbent was investigated using the Langmuir and Freundlich isotherm models. Adsorption on the various adsorption sites can be verified using the Freundlich model. This adsorption model is suitable for non-ideal procedures due to its variable adsorption energy, which also produces a complex heterogeneous surface on the adsorbent. [30] The isotherm profiles for the nonlinear Langmuir and Freundlich models for MB adsorption by the S-RFSi_SCD adsorbent are presented in Fig. 9(g) and 9(h), respectively, the isotherm parameter values for which are reported in Table S8. The maximum adsorption capacity (q_m) of S-RFSi_SCD for MB calculated using the nonlinear Langmuir adsorption model was 105.48 mg/g. Moreover, the R^2 value for the Langmuir model (~0.98) was much higher than that for the Freundlich model (0.67), thus confirming that MB dye adsorption on the S-RFSi aerogel is homogeneous.

The influence of temperature (25, 40, 60, and 80 °C) on the thermodynamic adsorption of MB on the S-RFSi aerogel is shown in Fig. 9(i). Table S9 reports the estimated values for the thermodynamic parameters for MB adsorption on the S-RFSi aerogel. The absence of spontaneous MB adsorption on the S-RFSi aerogel is shown by the positive ΔG° value, while the positive ΔH° value indicates that the adsorption process is endothermic. Furthermore, the positive ΔS° value indicates that the adsorption of MB on the S-RFSi aerogel involves physisorption, which suggests stable organized attachment of MB molecules. This type of interaction implies the loose binding of MB molecules on the active

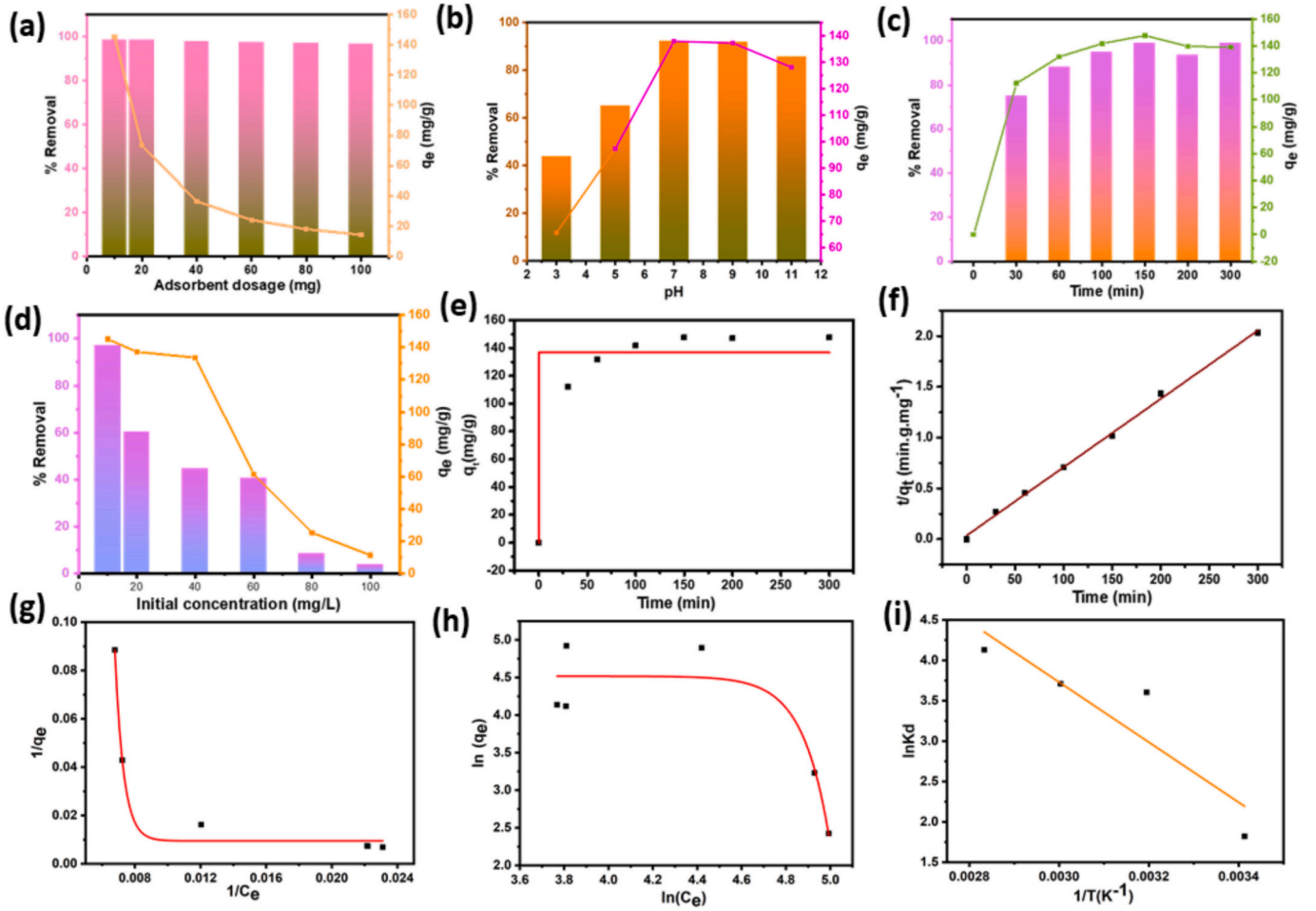

Fig. 9. Effects of (a) pH, (b) adsorbent amount, (c) contact time, and (d) initial concentration of MB dye solution on its adsorption by the S-RFSi_SCD aerogel. (d) Influence of adsorption time on the removal efficiency of MB by the S-RFSi_SCD aerogel. Fitted curves for the nonlinear pseudo-first-order (e) and linear pseudo-second-order (f) kinetic models. Isotherms for the adsorption of MB by the S-RFSi_SCD aerogel surface. (g) Nonlinear Langmuir isotherm model. (h) Nonlinear Freundlich isotherm model, and (i) Van't Hoff plot for the adsorption of MB on the S-RFSi_SCD aerogel.

adsorption sites in S-RFSi aerogel, thereby making it easy to remove them via desorption.

5.3. Selectivity, reusability and mechanism of adsorption

The competition adsorption of Pb^{2+}, Cd^{2+} and Hg^{2+} under optimal conditions (concentration, pH, temperature) for 30 min was investigated for S-RFSi_SCD aerogel. A selectivity toward Hg^{2+} was identified following $Hg^{2+} > Cd^{2+} > Pb^{2+}$ (Fig. 10a). This situation favours a stronger interaction between S-functional group and Hg^{2+} ions, and as a result, a better selectivity. The selective adsorption efficiencies of Hg^{2+} (97.756 %), Cd^{2+} (82.497 %), and Pb^{2+} (78.795 %) by S-functionalized RFSi aerogels can be rationalized by the synergistic effects of chemical affinity and ionic size. According to the hard–soft acid–base (HSAB) principle, sulfur is a soft Lewis base with strong binding preference for soft Lewis acids such as Hg^{2+}, leading to highly stable Hg—S coordination bonds and thus the highest removal efficiency. Cd^{2+}, with a comparable but slightly smaller ionic radius, also shows strong interaction with sulfur, resulting in moderately high adsorption. In contrast, Pb^{2+}, though borderline soft, has a larger ionic radius and weaker interaction with sulfur, which limits access to active sites and lowers its removal efficiency.

Fig. 10(b) presents the q_e and q_m values for Hg^{2+} and MB removal by the S-RFSi SCD aerogel adsorbent via pseudo-second-order and Langmuir models; it could adsorb Hg^{2+} with q_e and q_m values of ~1000 and ~ 699.3 mg/g, respectively, and MB with values of ~148.6 and ~ 105.48 mg/g, respectively. Thus, the aerogel adsorbent can efficiently remove both from industrial wastewater. The S-RFSi aerogels' capacity to be reused for HMI adsorption was assessed over five consecutive adsorption-desorption cycles under ideal circumstances, the results of which are presented in Fig. 10(c). After five cycles, the adsorption capacity for Hg^{2+} was maintained at 94.78 % efficiency. Table 2 reports a comparison of the S-RFSi aerogel adsorbent's HMI adsorption capability with those of previously reported ones; the former's Hg^{2+} capacity is on par with the best previously reported RF, RF/Si, and other aerogels [66–78]. This demonstrates the S-RFSi_SCD aerogel's exceptional ability to adsorb various HMIs from polluted water.

The reusability of S-RFSi_SCD for MB dye adsorption was studied to determine the durability of the former. The experimental results in Fig. 10(d) demonstrate that the efficacy of the S-RFSi aerogel (92.3 %) decreased by 7.7 % following five consecutive adsorption-desorption cycles. The results intimate that the S-RFSi aerogel adsorbent is eminently regeneratable and can be used to effectively remove MB dye molecules from water. The results for the S-RFSi aerogel adsorbent were compared with those of other previously reported adsorbents, as provided in Table 3; it can be seen that the S-RFSi_SCD aerogel adsorbent was more effective than the others [79–87].

Fig. 10(e) proves the durability of present aerogel adsorbent by confirming FTIR measurements before and after five consecutive adsorption-desorption cycles of MB. It was observed that the all bonding vibrations in FTIR spectra for S-RFSi_SCD aerogel adsorbent before adsorption and after five adsorption-desorption cycles. Epoxy-thiol

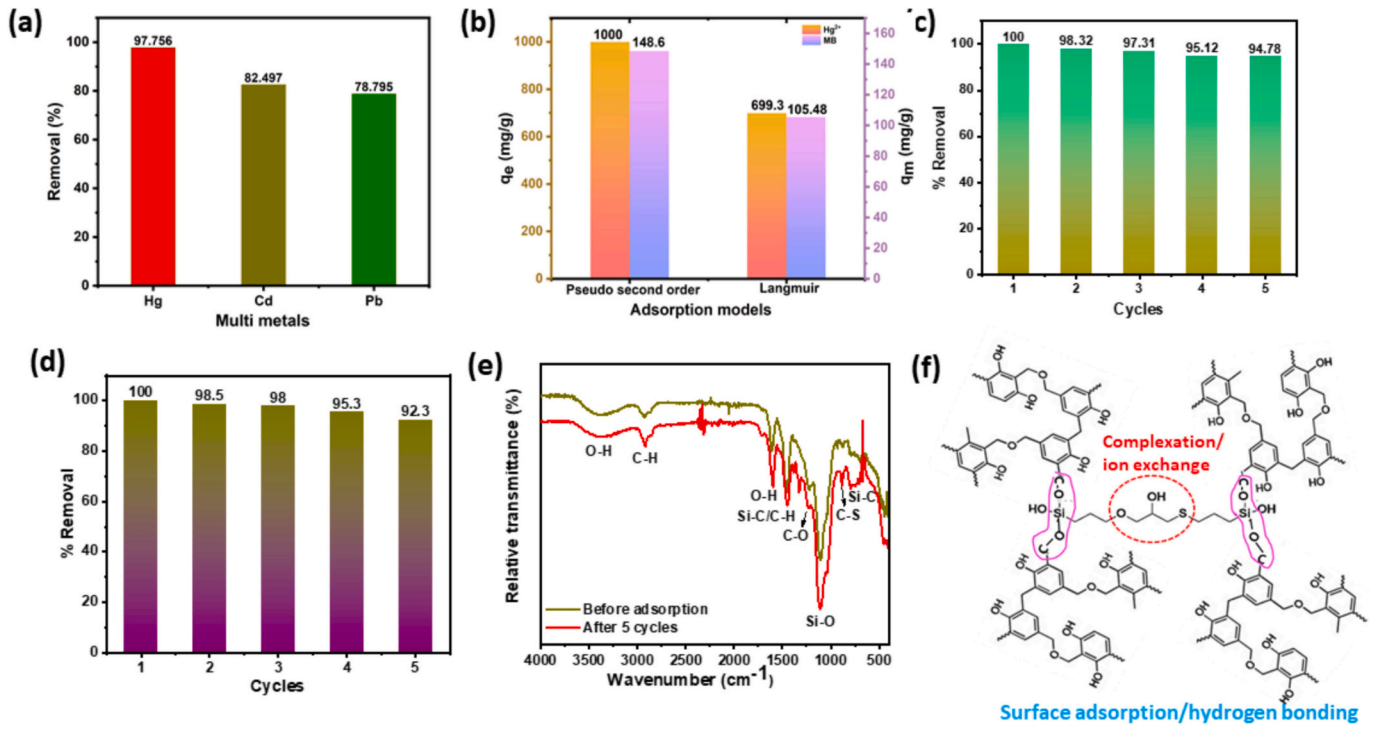

Fig. 10. (a) Selective Hg^{2+} removal by S-RFSi_SCD aerogel in Cd^{2+}, and Pb^{2+} metal mixtures, (b) Maximum adsorption capacities for Hg^{2+} and MB adsorption, Recycling performance of the S-RFSi_SCD aerogel for (c) Hg^{2+} and (d) MB adsorption., (e) FTIR spectra for the S-RFSi_SCD aerogel adsorbent before and after 5 consecutive adsorption-desorption cycles, and (e) possible Hg^{2+} and MB adsorption mechanisms.

Table 3
Comparison of the maximum adsorption capacities of the aerogel and MOF adsorbents for the MB.

Aerogel adsorbent	Dye solution	q_m (mg/g)	Ref.
CD-cellulose	MB	50	[79]
Hydrophobic silica	MB	65.74	[80]
Hydrophilic silica	MB	47.21	
Titania doped silica	MB	131.58	[81]
Cellulose@ZIF-8	RhB	40.4	[82]
Carbon fiber aerogel	MB	102.2	[83]
Cellulose aerogel	MB	29.7	[84]
keratin/silk fibroin	MB	163.84	[85]
P-shell MOF	MB	106.38	[86]
Zr-MOF	MB	89.2	[87]
S-RFSi	MB	105.48	This work

crosslinking in the S-RFSi_SCD aerogel provides a stable and robust network and makes functional groups available for interaction with HMIs and MB. The thiol groups have a strong affinity for Hg^{2+} ions. The S_RFSi aerogel is highly porous with a large number of accessible pores that provide numerous active sites for adsorption. Epoxy-thiol crosslinking provides both mechanical strength and flexibility, thereby enabling the aerogel to withstand multiple adsorption-desorption cycles without significant degradation. In addition, some reported aerogels lack specific functionality for HMI and MB adsorption and are mechanically fragile with poor long-term use. From all above findings, one can conclude that S-RFSi_SCD aerogel adsorbent is more efficient Hg^{2+} and MB dye adsorbent, takes a place with other adsorbents for future flow-water treatment applications.

The possible adsorption mechanism presented in Fig. 10(f) indicates that adsorption is due to complexation or ion exchange (via the S-functional groups), along with surface adsorption or hydrogen bonding (via the surface hydroxyl groups). Complexation results in HMIs forming strong bonds with functional groups on the adsorbent surface (-SH functional groups in present aerogels). In addition, metal ion exchange is via the surface functional groups on the adsorbent. However, MB is attracted toward negatively charged OH surface groups on the adsorbent, and hydrogen bonds form between them and the N atoms in MB.

XPS was employed to investigate the chemical structures of the S-RFSi_SCD aerogel. The survey scan spectrum [Fig. 11(a)] confirmed the presence of C 1 s, Si 2p, O 1 s, and S 2p peaks at 284.6, 102.0, 532.1, and 163.1 eV, respectively, along with an additional Hg 4f signal at 105.23 eV after Hg^{2+} adsorption [29,88]. High-resolution deconvoluted spectra of Si 2p, C 1 s, O 1 s, and S 2p are presented in Fig. 11(c–f) and (g-i) for before and after Hg^{2+} adsorption . In the Si 2p spectrum, two peaks at 101.9 and 102.7 eV correspond to Si—C and Si—O linkages, respectively [29]. The C 1 s spectrum displayed three peaks at 284.6, 285.5, and 288.5 eV, attributable to C—C (benzene ring carbons), C–O–H/C–O–C, and O–C=O bonds, respectively [88]. The distinct shoulder peak at 288.5 eV further evidences strong crosslinking between RF and epoxy–thiol–polymerized Si. The O 1 s spectrum exhibited two peaks at 532.0 and 533.3 eV, assigned to O—Si and O–C/O–H groups, respectively [30]. The S 2p spectrum revealed splitting into $S2p_{3/2}$ and $S2p_{1/2}$ peaks at 163.1 and 164.5 eV, confirming the successful epoxy–thiol polymerization reaction [29]. The $S2p_{1/2}$ component is associated with R–SH/C–SH functionalities, indicating thiol crosslinking in the aerogel [89]. These results collectively confirm strong chemical crosslinking between GPTMS- and MPTMS-derived Si units and the RF polymer.

Following Hg^{2+} ion adsorption (Fig. 11(b)), additional $Hg4f_{7/2}$ and $Hg4f_{5/2}$ peaks were detected at 101.62 and 105.23 eV, respectively, with a spin–orbit splitting of 3.61 eV. Deconvolution results indicate that Hg primarily exists in the +2-oxidation state within the S-RFSi_SCD aerogel pores [90]. Furthermore, the O 1 s spectrum demonstrated Hg—O interactions, suggesting that Hg^{2+} also coordinates with oxygen sites on the pore surfaces. Notably, the Si 2p peak remained largely unchanged, confirming that silica mainly serves as a structural support, while oxygen and sulfur moieties act as the active adsorption centers. Taken together, these findings suggest that the adsorption mechanism of Hg^{2+} onto S-RFSi aerogels arises from a synergistic effect between epoxy–thiol

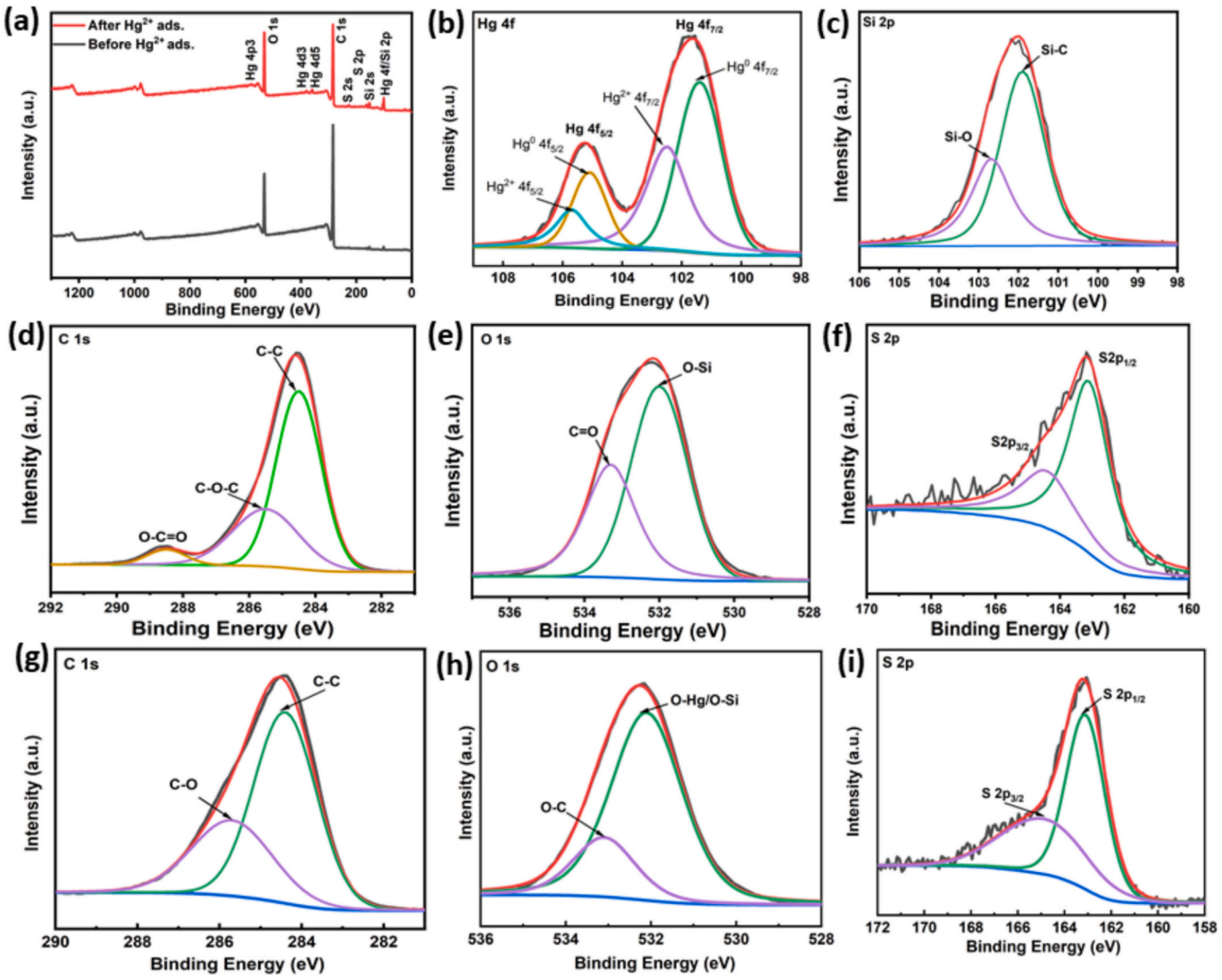

Fig. 11. XPS analysis of the S-RFSi_SCD aerogel: (a) survey scan and high-resolution (b) Hg 4f, (c) Si 2p, (d, g) C 1 s, (e, h) O 1 s, and (f, i) S 2p spectra before and after Hg^{2+} adsorption.

crosslinking and the sol–gel–derived porous network, which enables strong Hg—S and Hg—O interactions.

6. Conclusions

Mechanically strong yet flexible thick necked RFSi aerogels were fabricated by using epoxy-thiol polymerization and a sol-gel process. SEM and TEM images confirmed stronger and thicker particle necking enhancement in the S-RFSi_SCD aerogel than in other previously reported mechanically weak RF-Si composite aerogels. The presence of Si 2p and S 2p peaks in the XPS analysis confirmed that epoxy-thiol polymerization had proceeded successfully. Our approach enhanced the deformation and moving resistance of the aerogel while maintaining its flexibility. The addition of FEA simulations expanded the understanding of the structural mechanics and served as a validation tool, confirming that the designed neck structures are responsible for the mechanically strong yet flexible nature of the aerogels. The S-RFSi_SCD aerogel showed ultralow density (~0.050 g·cm^{-3}), high porosity (~96 %), large recoverable compressibility at 50 % strain, excellent fatigue resistance (an energy loss coefficient of 0.4), a high Young's modulus (5.65 MPa), and relatively low thermal conductivity (~0.026 W·m^{-1} K^{-1}) at room temperature, comparable to that of still air. The optimized S-RFSi aerogel is capable of both HMI and dye adsorption, with maximum Hg^{2+} adsorption of ~699.3 mg/g and moderate MB dye adsorption of ~105.48 mg/g. This excellent adsorption is due to the S-functional groups obtained via epoxy-thiol polymerization and surface hydroxyl groups. This study provides a new approach to designing functional hybrid organic-inorganic aerogels with excellent mechanical properties and high functionality for versatile applications in harsh environments.

CRediT authorship contribution statement

Vinayak G. Parale: Writing – original draft, Visualization, Methodology, Investigation, Data curation, Conceptualization. **Haryeong Choi:** Writing – original draft, Visualization, Validation, Methodology, Conceptualization. **Varsha D. Phadtare:** Validation, Investigation, Formal analysis. **Rushikesh P. Dhavale:** Validation, Formal analysis. **Younghun Kim:** Formal analysis. **Akshay A. Ransing:** Formal analysis. **Ivan I. Smalyukh:** Writing – review & editing, Data curation. **Michele Meo:** Writing – review & editing, Supervision, Resources. **Hyung-Ho Park:** Writing – review & editing, Supervision, Project administration, Funding acquisition.

Declaration of competing interest

The authors declare that they have no known competing financial interests or personal relationships that could have influenced the work reported in this paper.

Acknowledgments

This work was supported by the National Research Foundation of Korea (NRF) grant funded by the Korean government (MSIT) (No. 2020R1A5A1019131).

Appendix A. Supplementary data

Supplementary data to this article can be found online at https://doi.org/10.1016/j.cej.2025.170739.

Data availability

Data will be made available on reasonable request.

References

[1] V.G. Parale, T. Kim, H. Choi, V.D. Phadtare, R.P. Dhavale, K. Kanamori, H.-H. Park, Mechanically strengthened aerogels through multiscale, multicompositional, and multidimensional approaches: a review, Adv. Mater. 36 (2024) 2307772.
[2] X. Hou, J. Chen, Z. Chen, D. Yu, S. Zhu, T. Liu, L. Chen, Flexible aerogel materials: a review on revolutionary flexibility strategies and the multifunctional applications, ACS Nano 18 (2024) 11525–11559.
[3] L. Su, S. Jia, J. Ren, X. Lu, S.-W. Guo, P. Guo, Z. Cai, D. Lu, M. Niu, L. Zhuang, K. Peng, H. Wang, Strong yet flexible ceramic aerogel, Nat. Commun. 14 (2023) 7057.
[4] H. Su, Y. Liu, Q. Ren, Z. Shen, M. Guo, X. Li, J. Zhang, L. Liu, H. Fu, Unveiling the dynamic instability mechanism of microstructure transformation in faceted oxide eutectic composite ceramics, J. Mater. Sci. Technol. 144 (2023) 224–234.
[5] X.-C. Lin, S.-L. Li, W.-X. Li, Z.-H. Wang, J.-Y. Zhang, B.-W. Liu, T. Fu, H.-B. Zhao, Y.-Z. Wang, Thermo-responsive self-ceramifiable robust aerogel with exceptional strengthening and thermal insulating performance at ultrahigh temperatures, Adv. Funct. Mater. 33 (2023) 2214913.
[6] L. An, J. Wang, D. Petit, J.N. Armstrong, K. Hanson, J. Hamilton, M. Souza, D. Zhao, C. Li, Y. Liu, Y. Huang, Y. Hu, Z. Li, Z. Shao, A.O. Desjarlais, S. Ren, An all-ceramic, anisotropic, and flexible aerogel insulation material, Nano Lett. 20 (2020) 3828–3835.
[7] F. Liu, Y. Jiang, F. Peng, J. Feng, L. Li, J. Feng, Fiber-reinforced alumina-carbon core-shell aerogel composite with heat-induced gradient structure for thermal protection up to 1800 °C, Chem. Eng. J. 461 (2023) 141721.
[8] J. Zhang, R. Rajkhowa, J.L. Li, X.Y. Liu, X.G. Wang, Silkworm cocoon as natural material and structure for thermal insulation, Mater. Des. 49 (2013) 842–849.
[9] F. Chen, D. Porter, F. Vollrath, Morphology and structure of silkworm cocoons, Mater. Sci. Eng. C 32 (2012) 772–778.
[10] H.-P. Zhao, X.-Q. Feng, S.-W. Yu, W.-Z. Cui, F.-Z. Zou, Mechanical properties of silkworm cocoons, Polymer 46 (2005) 9192–9201.
[11] L. Su, M. Niu, D. Lu, Z. Cai, M. Li, H. Wang, A review on the emerging resilient and multifunctional ceramic aerogels, J. Mater. Sci. Technol. 75 (2021) 1–13.
[12] L. Su, H. Wang, S. Jia, S. Dai, M. Niu, J. Ren, X. Lu, Z. Cai, D. Lu, M. Li, L. Xu, S.-W. Guo, L. Zhuang, K. Peng, Highly stretchable, crack-insensitive and compressible ceramic aerogel, ACS Nano 15 (2021) 18354–18362.
[13] L.D. Hung Anh, Z. Pásztory, An overview of factors influencing thermal conductivity of building insulation materials, J. Build. Eng. 44 (2021) 102604.
[14] X. Xu, S. Fu, J. Guo, H. Li, Y. Huang, X. Duan, Elastic ceramic aerogels for thermal superinsulation under extreme conditions, Mater. Today 42 (2021) 162–177.
[15] L. Zhou, L. Wu, T. Wu, D. Chen, X. Yang, G. Sui, A 'ceramer' aerogel with unique bicontinuous inorganic–organic structure enabling super-resilience, hydrophobicity, and thermal insulation, Materials Today Nano 22 (2023) 100306.
[16] S. Iswar, S. Galmarini, L. Bonanomi, J. Wernery, E. Roumeli, S. Nimalshantha, A. M. Ben Ishai, M. Lattuada, M.M. Koebel, W.J. Malfait, Dense and strong, but superinsulating silica aerogel, Acta Mater. 213 (2021) 116959.
[17] Q. Liu, Z. Lu, M. Zhu, Z. Yuan, Z. Yang, Z. Hu, J. Li, Simulation of the tensile properties of silica aerogels: the effects of cluster structure and primary particle size, Soft Matter 10 (2014) 6266–6277.
[18] S. Iswar, W.J. Malfait, S. Balog, F. Winnefeld, M. Lattuada, M.M. Koebel, Effect of aging on silica aerogel properties, Microporous Mesoporous Mater. 241 (2017) 293–302.
[19] V.G. Parale, W. Han, H.-N.-R. Jung, K.-Y. Lee, H.-H. Park, Ambient pressure dried tetrapropoxysilane-based silica aerogels with high specific surface area, Solid State Sci. 75 (2018) 63–70.
[20] V.G. Parale, K.-Y. Lee, H.-H. Park, Flexible and transparent silica aerogels: An overview, J. Korean Ceram. Soc. 54 (2017) 184–199.
[21] V.G. Parale, K.-Y. Lee, H.-N.-R. Jung, H.-Y. Nah, H. Choi, T.-H. Kim, V.D. Phadtare, H.-H. Park, Facile synthesis of hydrophobic, thermally stable, and insulative organically modified silica aerogels using co-precursor method, Ceram. Int. 44 (2018) 3966–3972.
[22] H. Choi, V.G. Parale, T. Kim, Y.-S. Choi, J. Tae, H.-H. Park, Structural and mechanical properties of hybrid silica aerogel formed using triethoxy(1-phenylethenyl)silane, Microporous Mesoporous Mater. 298 (2020) 110092.
[23] X. Long, X. Yan, L. Zhou, W. Chen, S. Ren, Y. Qiu, L. Sui, X. Wei, S. Wang, J. Liao, Highly deformable high-strength SiO2 aerogel designed with an alternating structure of hard cores and flexible chains for thermal insulation, ACS Macro Lett. 12 (2023) 653–658.
[24] T. Huang, Y. Zhu, J. Zhu, H. Yu, Q. Zhang, M. Zhu, Self-reinforcement of light, temperature-resistant silica nanofibrous aerogels with tunable mechanical properties, Adv. Fiber Mater. 2 (2020) 338–347.
[25] X. Cheng, Y.-T. Liu, Y. Si, J. Yu, B. Ding, Direct synthesis of highly stretchable ceramic nanofibrous aerogels via 3D reaction electrospinning, Nat. Commun. 13 (2022) 2637.
[26] C. Liu, S. Wang, N. Wang, J. Yu, Y.-T. Liu, B. Ding, From 1D nanofibers to 3D Nanofibrous aerogels: a Marvellous evolution of electrospun SiO2 nanofibers for emerging applications, Nano-Micro Letters 14 (2022) 194.
[27] J. Liu, J. Liu, F. Shi, C. Ma, T. Li, C. Chen, M. Wasim, K. Zhu, H. Sun, Z. Tian, A facile pore size controlling strategy to construct rigid/flexible silica aerogels for super heat insulation and VOCs adsorption, Chem. Eng. J. 450 (2022) 138196.
[28] H. Choi, H.H. Han, V.G. Parale, T. Kim, W. Park, Y. Kim, J. Kim, Y. Choi, Y.-S. Bae, H.-H. Park, Rigid amine-incorporated silica aerogel for highly efficient CO2 capture and heavy metal removal, Chem. Eng. J. 483 (2024) 149357.
[29] V.G. Parale, H. Choi, T. Kim, V.D. Phadtare, R.P. Dhavale, K.-Y. Lee, A. Panda, H.-H. Park, One pot synthesis of hybrid silica aerogels with improved mechanical properties and heavy metal adsorption: synergistic effect of in situ epoxy-thiol polymerization and sol-gel process, Sep. Purif. Technol. 308 (2023) 122934.
[30] R.P. Dhavale, V.G. Parale, H. Choi, T. Kim, K.-Y. Lee, V.D. Phadtare, H.-H. Park, Epoxy-thiol crosslinking for enhanced mechanical strength in silica aerogels and highly efficient dye adsorption, Appl. Surf. Sci. 642 (2024) 158619.
[31] F. Akhter, S. Ahmed, J. Ahmed, M.J. Ahsan, H.J. Arain, M.A. Lakhmir, Evaluating Pb (II) adsorption performance by amine-modified resorcinol formaldehyde aerogel and organically modified silica aerogel: comparative study of adsorption, synthesis, characterization, and isotherms, Biomass Convers. Biorefinery 14 (2023) 31631–31641.
[32] A. Yazdanbakhsh, A. Behzadi, A. Moghaddam, I. Salahshoori, H.A. Khonakdar, Mechanisms and factors affecting the removal of minocycline from aqueous solutions using graphene-modified resorcinol formaldehyde aerogels, Sci. Rep. 13 (2023) 22771.
[33] S. Motahari, M. Nodeh, K. Maghsoudi, Absorption of heavy metals using resorcinol formaldehyde aerogel modified with amine groups, Desalin. Water Treat. 57 (2016) 16886–16897.
[34] L. Keshavarz, M.R. Ghaani, N.J. English, The importance of precursors and modification groups of aerogels in CO2 capture, Molecules 26 (2021) 5023.
[35] M. Sadat-Shojai, A. Keshavarzi, M. Asadnia, Heavy metals removal from aqueous solution using resorcinol-formaldehyde matrix incorporated with hydroxyapatite nanoparticles, J. Sol-Gel Sci. Technol. 108 (2023) 466–476.
[36] L. Wang, J. Wang, L. Zheng, Z. Li, L. Wu, X. Wang, Superelastic, anticorrosive, and flame-resistant nitrogen-containing resorcinol formaldehyde/graphene oxide composite aerogels, ACS Sustain. Chem. Eng. 7 (2019) 10873–10879.
[37] S. Yun, H. Luo, Y. Gao, Ambient-pressure drying synthesis of large resorcinol–formaldehyde-reinforced silica aerogels with enhanced mechanical strength and superhydrophobicity, J Mater Chem A 2 (2014) 14542–14549.
[38] S. Berthon-Fabry, C. Hildenbrand, P. Ilbizian, E. Jones, S. Tavera, Evaluation of lightweight and flexible insulating aerogel blankets based on resorcinol-formaldehyde-silica for space applications, Eur. Polym. J. 93 (2017) 403–416.
[39] Y. Cheng, J. Zhang, C. Ren, S. Zhao, X. Zhang, J. Fan, Facile preparation of high-strength SiC/C aerogels from pre-reacted resorcinol–formaldehyde and siloxane, J. Ind. Eng. Chem. 134 (2024) 75–83.
[40] F. Li, J. Song, Y. Niu, H. Zhang, M. Niederberger, W. Cheng, Superelastic cobalt silicate@resorcinol formaldehyde resin Core-Shell Nanobelt aerogel monoliths with outstanding fire retardant and thermal insulating capability, Small 19 (2023) 2302724.
[41] M. Alshrah, H.E. Naguib, C.B. Park, Reinforced resorcinol formaldehyde aerogel with co-assembled polyacrylonitrile nanofibers and graphene oxide nanosheets, Mater. Des. 151 (2018) 154–163.
[42] B. Liu, W. Ju, J. Zhang, H. Fan, Q. Wang, X. Yi, Z. Yu, X. Wang, Improvement of mechanical strength of ultralight resorcinol–formaldehyde/silica aerogel by addition of zirconia, J. Sol-Gel Sci. Technol. 83 (2017) 100–108.
[43] S. Salimian, A. Zadhoush, Z. Talebi, B. Fischer, P. Winiger, F. Winnefeld, S. Zhao, M. Barbezat, M.M. Koebel, W.J. Malfait, Silica aerogel−epoxy nanocomposites: understanding epoxy reinforcement in terms of aerogel surface chemistry and epoxy−silica interface compatibility, ACS Appl. Nano Mater. 1 (2018) 4179–4189.
[44] D. Gong, M. Qu, X. Wang, X. Ai, P. Tang, W. Zhao, X. Wang, Y. Bin, Preparation of epoxy-enhanced silica aerogels with thermal insulation and hydrophobicity by ambient pressure drying, ACS Appl. Polymer Materials 7 (2025) 2997–3007.
[45] A. Albooyeh, P. Soleymani, H. Taghipoor, Evaluation of the mechanical properties of hydroxyapatite-silica aerogel/epoxy nanocomposites: optimizing by response surface approach, J. Mech. Behav. Biomed. Mater. 136 (2022) 105513.
[46] M.A.B. Meador, E.F. Fabrizio, F. Ilhan, A. Dass, G. Zhang, P. Vassilaras, J. C. Johnston, N. Leventis, Cross-linking amine-modified silica aerogels with epoxies: mechanically strong lightweight porous materials, Chem. Mater. 17 (2005) 1085–1098.

[47] S. Karamikamkar, M. Fashandi, H.E. Naguib, C.B. Park, In situ Interface Design in Graphene-Embedded Polymeric Silica Aerogel with organic/inorganic hybridization, ACS Appl. Mater. Interfaces 12 (2020) 26635–26648.
[48] Y. Shiraishi, T. Hagi, M. Matsumoto, S. Tanaka, S. Ichikawa, T. Hirai, Solar-to-hydrogen peroxide energy conversion on resorcinol–formaldehyde resin photocatalysts prepared by acid-catalysed polycondensation, Communications Chemistry 3 (2020) 169.
[49] Y. Kong, Y. Zhong, X. Shen, S. Cui, M. Fan, Effect of silica sources on nanostructures of resorcinol–formaldehyde/silica and carbon/silicon carbide composite aerogels, Microporous Mesoporous Mater. 197 (2014) 77–82.
[50] M. Lian, W. Ding, S. Liu, Y. Wang, T. Zhu, Y.-E. Miao, C. Zhang, T. Liu, Highly porous yet transparent mechanically flexible aerogels realizing solar-thermal regulatory cooling, Nano-Micro Letters 16 (2024) 131.
[51] M. Li, Z. Qin, Y. Cui, C. Yang, C. Deng, Y. Wang, J.S. Kang, H. Xia, Y. Hu, Ultralight and flexible monolithic polymer aerogel with extraordinary thermal insulation by a facile ambient process, Adv. Mater. Interfaces 6 (2019) 1900314.
[52] I.I. Smalyukh, Thermal management by engineering the alignment of Nanocellulose, Adv. Mater. 33 (2020) 2001228.
[53] S. Tan, J. Li, L. Zhou, P. Chen, D. Xu, Z. Xu, Fabrication of a flexible film electrode based on cellulose nanofibers aerogel dispersed with functionalized graphene decorated with SnO2 for supercapacitors, J. Mater. Sci. 53 (2018) 11648–11658.
[54] K. Chen, Z. Bao, A. Du, X. Zhu, J. Shen, G. Wu, Z. Zhang, B. Zhou, One-pot synthesis, characterization and properties of acid-catalyzed resorcinol/formaldehyde cross-linked silica aerogels and their conversion to hierarchical porous carbon monoliths, J. Sol-Gel Sci. Technol. 62 (2012) 294–303.
[55] A. Munir, T.u. Haq, A. Qurashi, H.u. Rehman, A. Ul-Hamid, I. Hussain, Ultrasmall Ni/NiO nanoclusters on thiol-functionalized and -exfoliated graphene oxide nanosheets for durable oxygen evolution reaction, ACS Appl Energy Mater 2 (2019) 363–371.
[56] M.A. Einarsrud, E. Nilsen, A. Rigacci, G.M. Pajonk, S. Buathier, D. Valette, M. Durant, B. Chevalier, P. Nitz, F. Ehrburger-Dolle, Strengthening of silica gels and aerogels by washing and aging processes, J. Non-Cryst. Solids 285 (2001) 1–7.
[57] R. Ueoka, Y. Hara, A. Maeno, H. Kaji, K. Nakanishi, K. Kanamori, Unusual flexibility of transparent poly(methylsilsesquioxane) aerogels by surfactant-induced mesoscopic fiber-like assembly, Nat. Commun. 15 (2024) 461.
[58] M. Alshrah, M.-P. Tran, P. Gong, H.E. Naguib, C.B. Park, Development of high-porosity resorcinol-formaldehyde aerogels with enhanced mechanical properties through improved particle necking under CO2 supercritical conditions, J. Colloid Interface Sci. 485 (2017) 65–74.
[59] Y. Si, X. Wang, L. Dou, J. Yu, B. Ding, Ultralight and fire-resistant ceramic nanofibrous aerogels with temperature-invariant superelasticity, Sci. Adv. 4 (2018) eaas8925.
[60] M. Schwan, R. Tannert, L. Ratke, New soft and spongy resorcinol–formaldehyde aerogels, J. Supercritical Fluid 107 (2016) 201–208.
[61] S. Yun, T. Guo, X. Zhu, L. Zhang, J. Zhang, X. Gao, Y. Gao, Effects of carbonization temperature on structure and mechanical properties of monolithic C/SiO2 aerogels based on ambient pressure dried superhydrophobic resorcinol–formaldehyde/SiO2 aerogels, J. Porous. Mater. 25 (2018) 1825–1830.
[62] J. Ren, T. Zhang, Y. Kong, Z. Zhao, K. Zhu, X. Zhang, X. Shen, Facile synthesis of phenolic-reinforced silica aerogel composites for thermal insulation under thermal-force coupling conditions, Ceram. Int. 49 (2023) 29820–29828.
[63] C. Wu, H. Huang, X. Jin, X. Yan, H. Wang, Y. Pan, X. Zhang, C. Hong, Water-assisted synthesis of phenolic aerogel with superior compression and thermal insulation performance enabled by thick-united nano-structure, Chem. Eng. J. 464 (2023) 142805.
[64] J. Yan, M. Kuang, Y. Zhu, Y. Chen, C. Zhang, H. Ma, X. Zhang, L. Kong, Facile, tunable, and environmental friendly synthesis of silica/resorcinol–formaldehyde hybrid xerogels with ultra-low shrinkage using a cationic polyelectrolyte as a soft template, J. Porous. Mater. 30 (2023) 103–113.
[65] M.A. Boles, M. Engel, D.V. Talapin, Self-assembly of colloidal nanocrystals: from intricate structures to functional materials, Chem. Rev. 116 (2016) 11220–11289.
[66] S. Zhang, X. Han, H. Cai, X. Wu, Y. Yuan, Y. Zhang, Aramid nanofibers/WS2 nanosheets co-assembled aerogels for efficient and stable Pb (II) adsorption in harsh environments, Chem. Eng. J. 450 (2022) 138268.
[67] Q. Wang, Y. Tian, L. Kong, J. Zhang, W. Zuo, Y. Li, G. Cai, A novel 3D superelastic polyethyleneimine functionalized chitosan aerogels for selective removal of Cr(VI) from aqueous solution: performance and mechanisms, Chem. Eng. J. 425 (2021) 137122.
[68] J. Liu, M. Chen, J. Sheng, J. Xu, Y. Shi, H. Jiang, Adsorption and co-adsorption mechanisms of p-nitrophenol and Pb(ii) on magnetic carbon aerogel in water, Environ. Sci. Water Res. Technol. 8 (2022) 820–835.
[69] Q. Wang, L. Li, Y. Tian, L. Kong, G. Cai, H. Zhang, J. Zhang, W. Zuo, B. Wen, Shapeable amino-functionalized sodium alginate aerogel for high-performance adsorption of Cr(VI) and cd(II): experimental and theoretical investigations, Chem. Eng. J. 446 (2022) 137430.
[70] B.S. Heidari, V.S. Cheraghchi, S. Matahari, G.H. Motlagh, S.M. Davachi, Optimized mercapto-modified resorcinol formaldehyde xerogel for adsorption of lead and copper ions from aqueous solutions, J. Sol-Gel Sci. Tech. 88 (2018) 236–248.
[71] S. Matahari, B.S. Heidari, G.H. Motlagh, Resorcinol formaldehyde xerogels modified with mercapto functional groups as mercury adsorbent, J. Appl. Polym. Sci. 132 (2015) 42543.
[72] F. Akhtar, S. Ahmed, J. Ahmed, M.J. Ahsan, H.J. Arain, M.A. Lakhmir, Biomass Convers. Biorefinery 14 (2024) 31631–31641.
[73] N.K. Verma, P. Khare, N. Verma, Synthesis of iron-doped resorcinol formaldehyde-based aerogels for the removal of Cr(VI) from water, green processing synthesis 4 (2015) 37–46.
[74] S. Motahhari, M. Nodeh, K. Maghsoudi, Absorption of heavy metals using resorcinol formaldehyde aerogel modified with amine groups, Desalin. Water Treat. 57 (2016) 16886–16897.
[75] T. Wu, H. Karimi-Maleh, Y. Li, D. Zhang, Z. Zhang, N. Zhong, Y. Wen, T. M. Aminabhavi, 3D printed porous chitosan/metal–organic framework composites as effective adsorbents to remove heavy metals from wastewater, Chem. Eng. J. 473 (2024) 152780.
[76] W.S. Abo Il Yazeed, Y.G. Abou El-Reash, L.A. Elatwy, Awad I. Ahmed, Facile fabrication of bimetallic Fe–Mg MOF for the synthesis of xanthenes and removal of heavy metal ions, RSC Adv. 10 (2020) 9693.
[77] M.N. Nimbalkar, B.R. Bhat, Simultaneous adsorption of methylene blue and heavy metals from water using Zr-MOF having free carboxylic group, J. Environ. Chem. Eng. 9 (2021) 106216.
[78] E. Ragheb, M. Shamsipur, F. Jalali, F. Mousavi, Modified magnetic-metal organic framework as a green and efficient adsorbent for removal of heavy metals, J. Environ. Chem. Engg. 10 (2022) 107297.
[79] D.G. Maldonado, A.M. Reynolds, L. Johansson, D.J. Burnett, J.B. Ramapuram, M. N. Waters, I.B.V. Erramuspe, M.S. Peresin, Fabrication of aerogels from cellulose nanofibril grafted with β-cyclodextrin for capture of water pollutants, J. Porous. Mater. 28 (2021) 1725–1736.
[80] H. Han, W. Wei, Z. Jiang, J. Lu, J. Zhu, J. Xie, Removal of cationic dyes from aqueous solution by adsorption onto hydrophobic/hydrophilic silica aerogel, Colloids Surf. A Physicochem. Eng. Asp. 509 (2016) 539–549.
[81] P.D. Sarvalkar, A.S. Vadanagekar, O.S. Karvekar, P.D. Kumbhar, S.S. Terdale, A. S. Thounajam, S.S. Kolekar, R.S. Vhatkar, P.S. Patil, K.K. Sharma, Thermodynamics of azo dye adsorption on a newly synthesized Titania-doped silica aerogel by cogelation: a comparative investigation with silica aerogels and activated charcoal, ACS Omega 8 (2023) 13285–13299.
[82] G. Wu, C. Zhou, H. Li, S. Xia, Y. Zhu, J. Han, W. Xing, Controlled fabrication of the biomass cellulose aerogel@ZIF-8 nanocomposite as efficient and recyclable adsorbents for methylene blue removal, Ind. Crop. Prod. 193 (2023) 116169.
[83] Z. Li, Z. Jia, T. Ni, S. Li, Adsorption of methylene blue on natural cotton based flexible carbon fiber aerogels activated by novel air-limited carbonization method, J. Mol. Liq. 242 (2017) 747–756.
[84] H.V. Le, N.T. Dao, H.T. Bui, P.T. Kim, K.A. Le, A.T. Tuong Tran Le, K.D. Nguyen, H. H. Mai Nguyen, P.H. Ho, Bacterial Cellulose Aerogels Derived from Pineapple Peel Waste for the Adsorption of Dyes, ACS Omega 8 (2023) 33412–33425.
[85] X. Xing, X. Zhang, Y. Feng, X. Yang, Adsorption of methylene blue dye on feather keratin/silk fibroin porous aerogels, J. Taiwan Inst. Chem. Eng. 166 (2025) 105298.
[86] S. Hegazy, H.H. Ibrahim, T. Weckman, T. Hu, S. Tuomikoski, U. Lassi, K. Honkala, V. Srivastava, Synergistic pyrolysis of cellulose/Fe-MOF composite: a combined experimental and DFT study on dye removal, Chem. Eng. J. 504 (2025) 158654.
[87] L. Shen, F. Guo, Y. Hang, J. Yang, Z. Guo, W. Liang, P. Du, W. Jiao, Synthesis of zirconium-based metal-organic framework under mild conditions and its application to the removal of cationic and anionic dyes from wastewater, J. Phys. Chem. Solids 198 (2025) 112452.
[88] V.G. Parale, T. Kim, K.-Y. Lee, V.D. Phadtare, R.P. Dhavale, H.-N.-R. Jung, H.-H. Park, Hydrophobic TiO_2–SiO_2 composite aerogels synthesized via in situ epoxy-ring opening polymerization and sol-gel process for enhanced degradation activity, Ceram. Int. 46 (2020) 4939–4946.
[89] E. Ren, C. Cui, J. Zhai, A. Li, H. Tang, B. Peng, R. Guo, H. Xiao, M. Zhou, J. Zhang, Facile synthesis of V2CTx@RGO composite aerogel via hydrothermal reaction and its dye adsorption performance, J. Mater. Sci. Mater. Electron. 34 (2023) 343.
[90] X. Li, Z. Lin, H. Lu, Y. Li, X. Chen, S. Zhu, Z. Zia, H.-W. Tan, Y. Yang, L.-A. Hou, Amorphization strategy for constructing metal-Triazole framework glass foams with multistage pore structure for selective removal of mercury, Adv. Funct. Mater. 35 (2025) 2501311.